Supporting Information

Functionalised organometallic photoswitches containing dihydropyrene units

Angus A. Gillespie,[a] Max Roemer,[b] David Jago,[a] Alexandre N. Sobolev,[c] Gareth L. Nealon,[c] Peter R. Spackman,[d] Stephen Moggach,[a] and George A. Koutsantonis*,[a]

[a]Chemistry, School of Molecular Science, The University of Western Australia, Crawley, WA 6009, Australia.

[b]School of Chemistry, The University of Sydney, Sydney, NSW 2006, Australia

[c]Centre for Microscopy, Characterisation and Analysis, The University of Western Australia, Crawley, WA 6009, Australia .

[d]Curtin Institute for Computation, School of Molecular and Life Sciences, Curtin University, GPO Box U1987, Perth, Western Australia 6845, Australia.

Table of Contents

Spectra

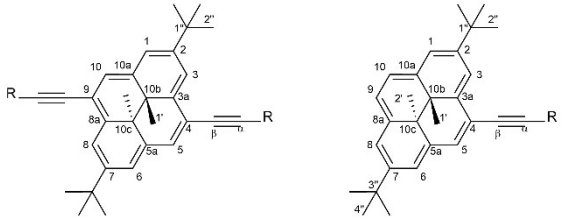

Figure S1 General numbering scheme for DHP and DHP complexes

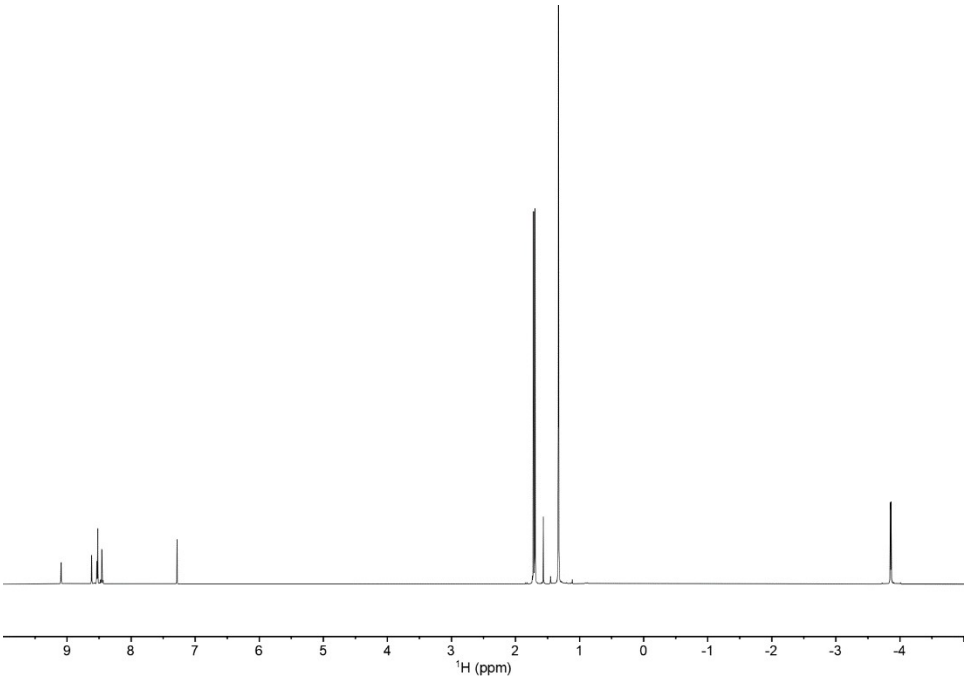

Figure S2 ^{1}H NMR spectrum of **3b** (500 MHz, $CDCl_3$)

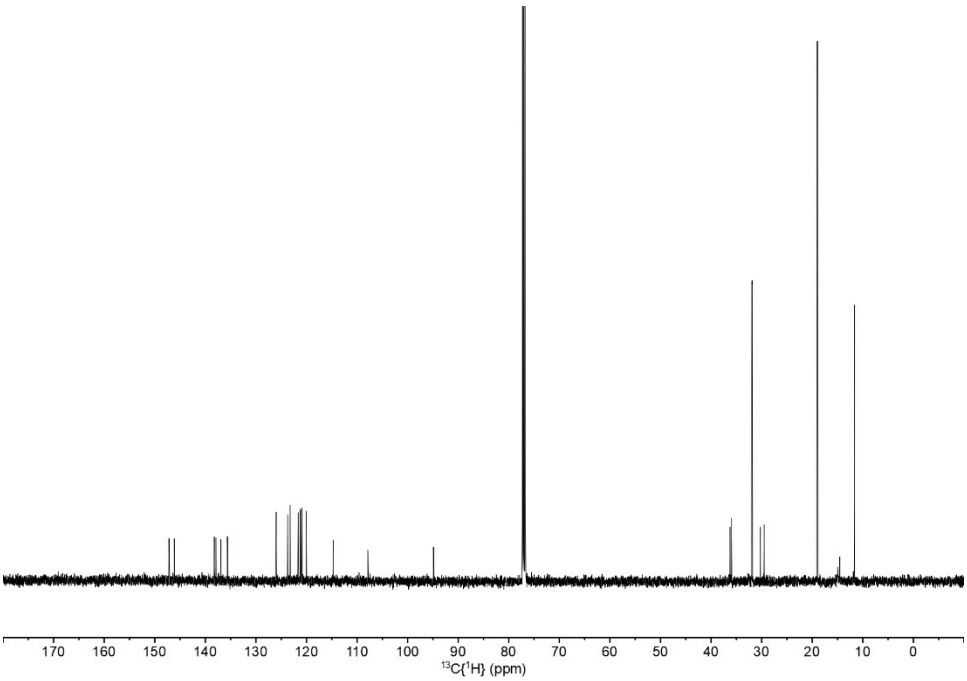

Figure S3 ^{13}C{^{1}H} NMR spectrum of **3b** (126 MHz, $CDCl_3$)

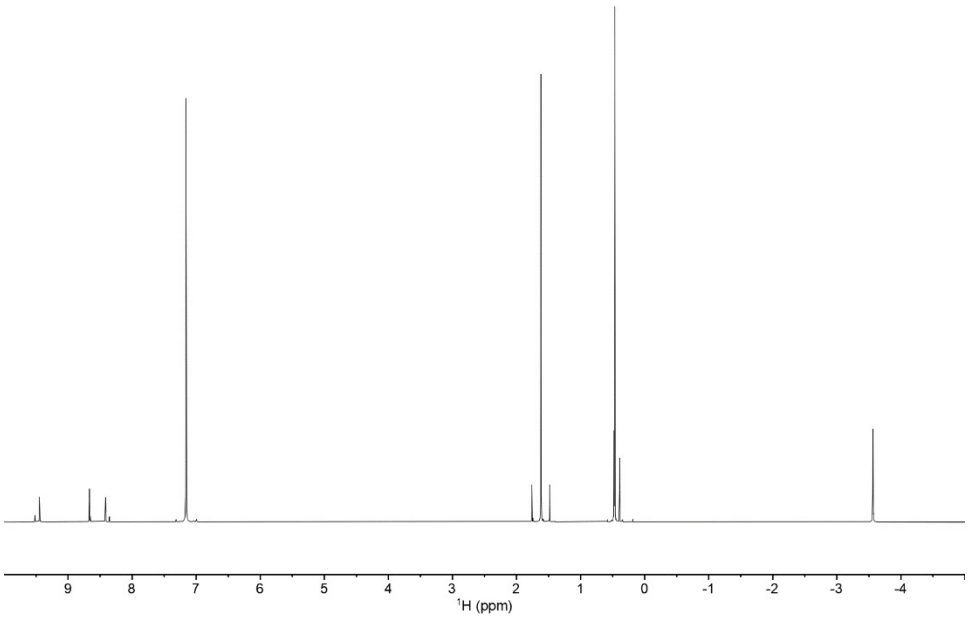

Figure S4 ^{1}H NMR spectrum of **3c** (500 MHz, C_6D_6)

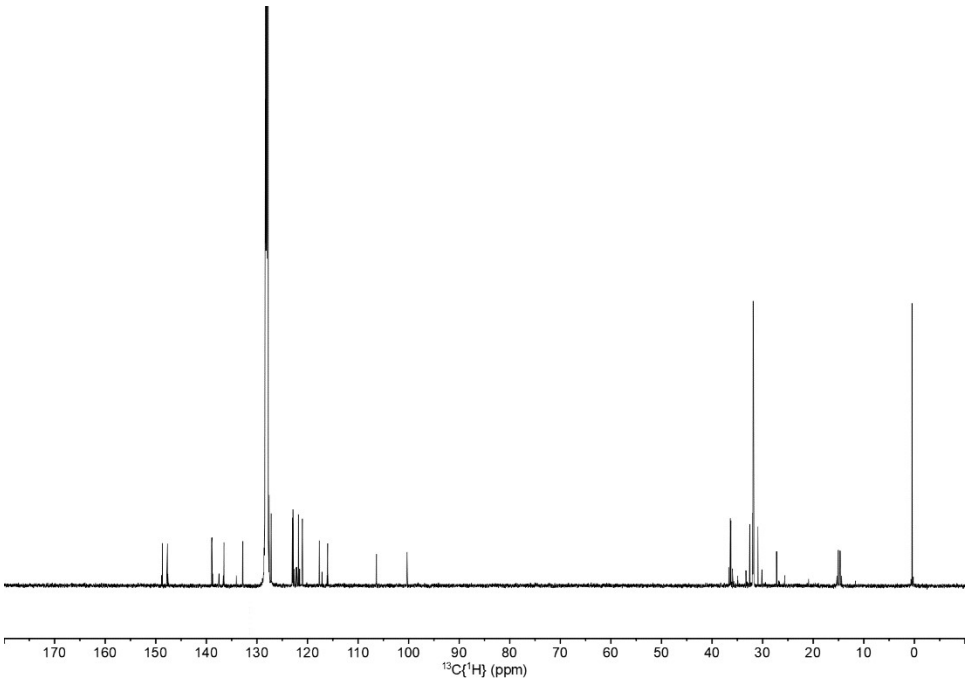

Figure S5 $^{13}C\{^{1}H\}$ NMR spectrum of **3c** (126 MHz, C_6D_6)

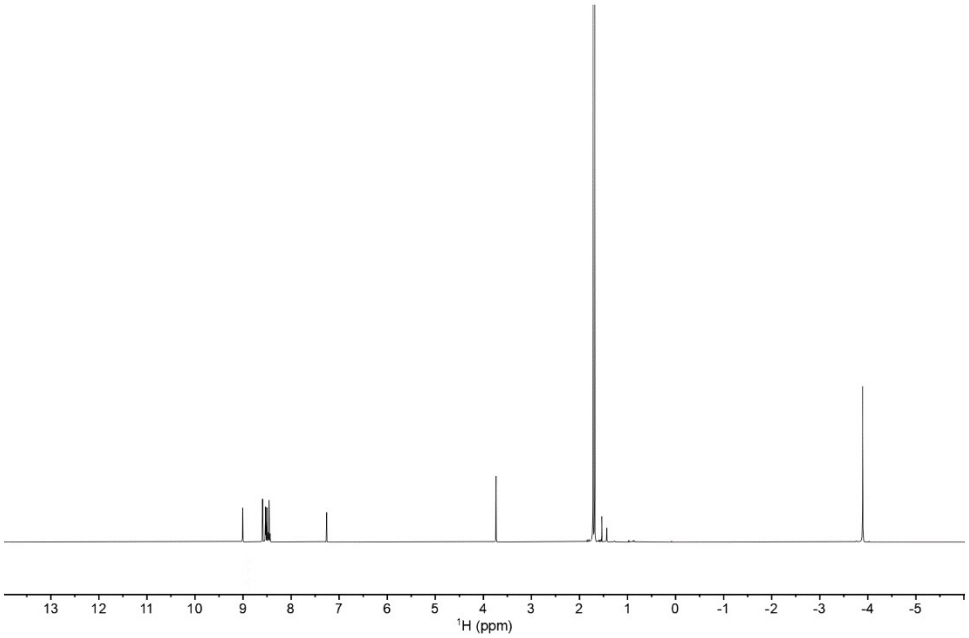

Figure S6 ^{1}H NMR spectrum of **4** (500 MHz, $CDCl_3$)

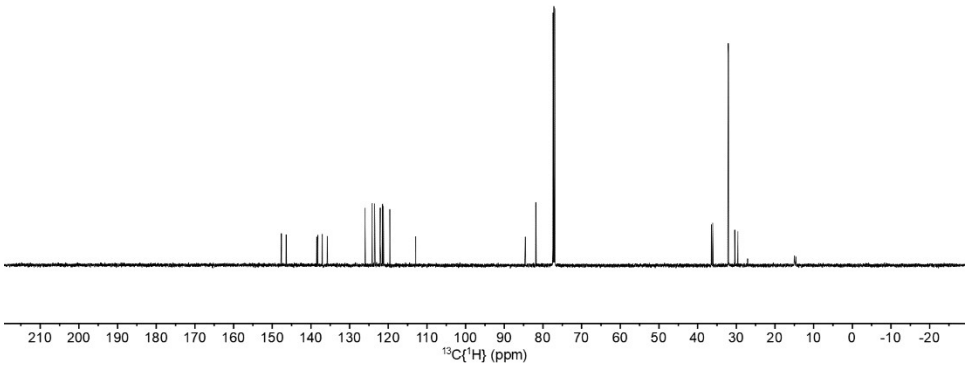

Figure S7 $^{13}C\{^{1}H\}$ NMR spectrum of **4** (126 MHz, $CDCl_3$)

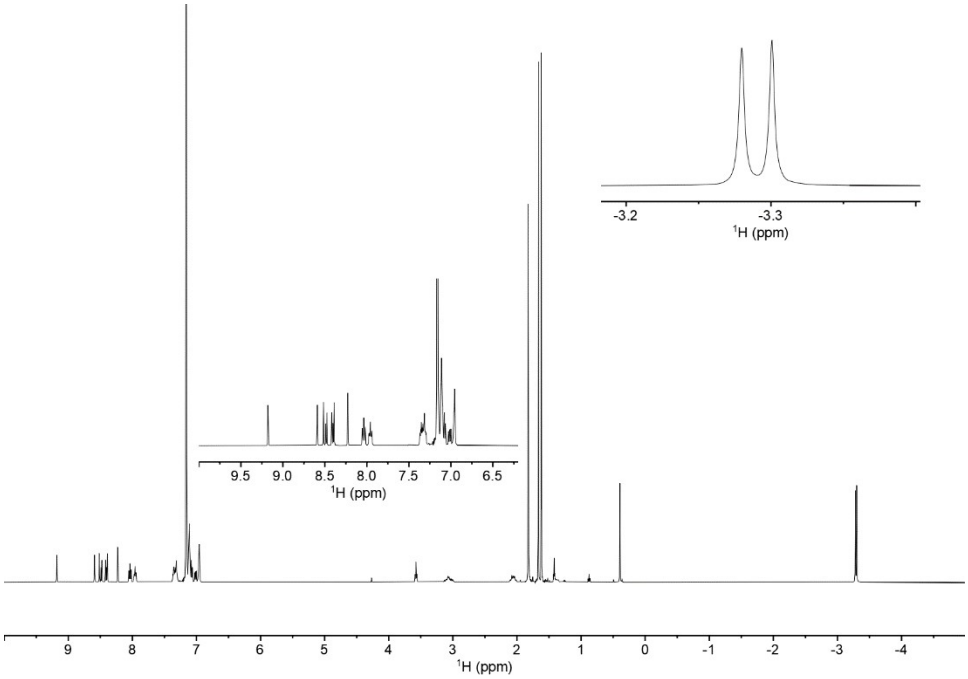

Figure S8 ^{1}H NMR spectrum of **Ru1** (500 MHz, C6D6)

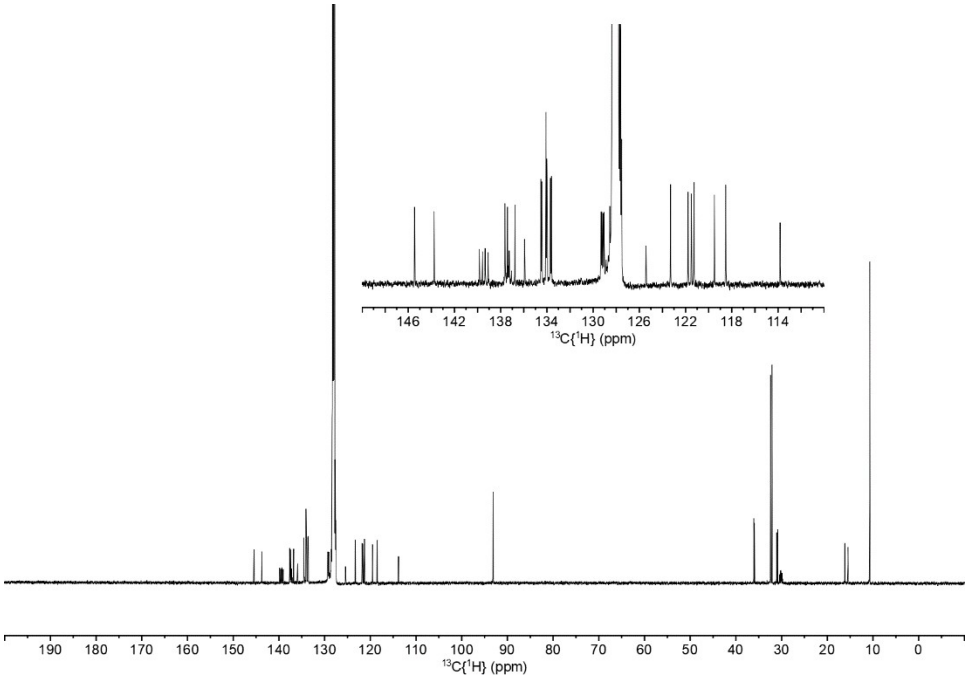

Figure S9 ^{13}C{^{1}H} NMR spectrum of **Ru1** (500 MHz, C_6D_6)

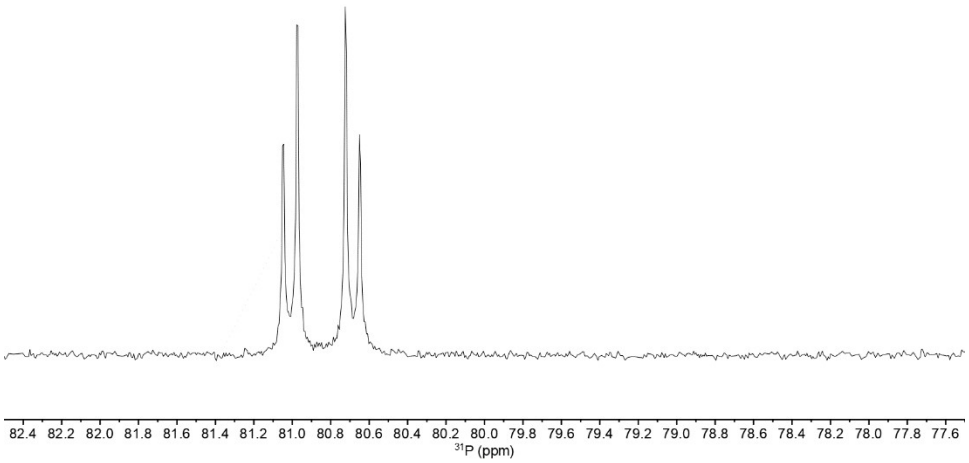

Figure S10 $^{31}P\{^{1}H\}$ NMR spectrum of **Ru1** (202 MHz, C_6D_6)

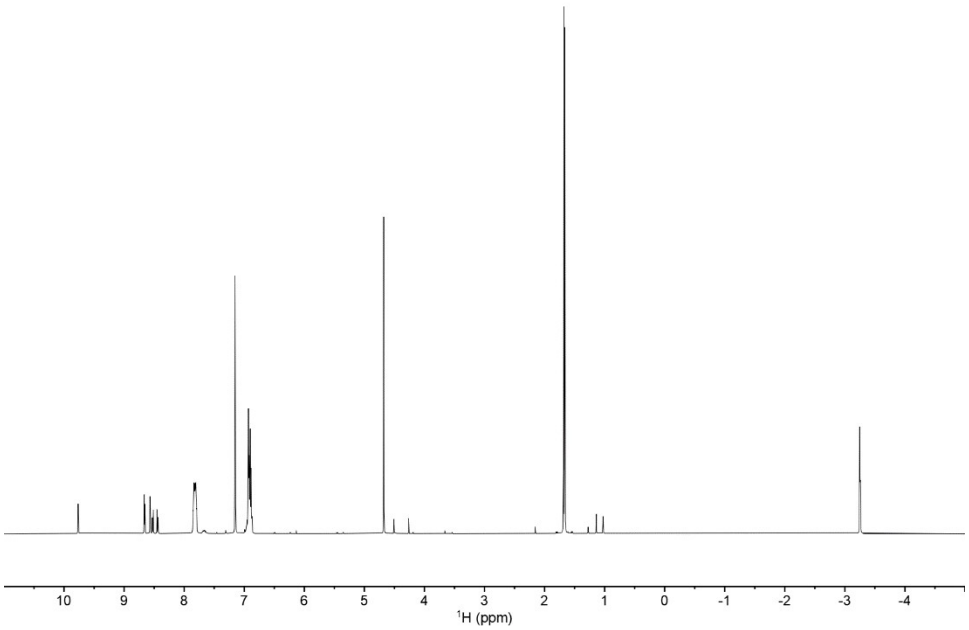

Figure S11 ^{1}H NMR spectrum of **Ru2** (500 MHz, C_6D_6)

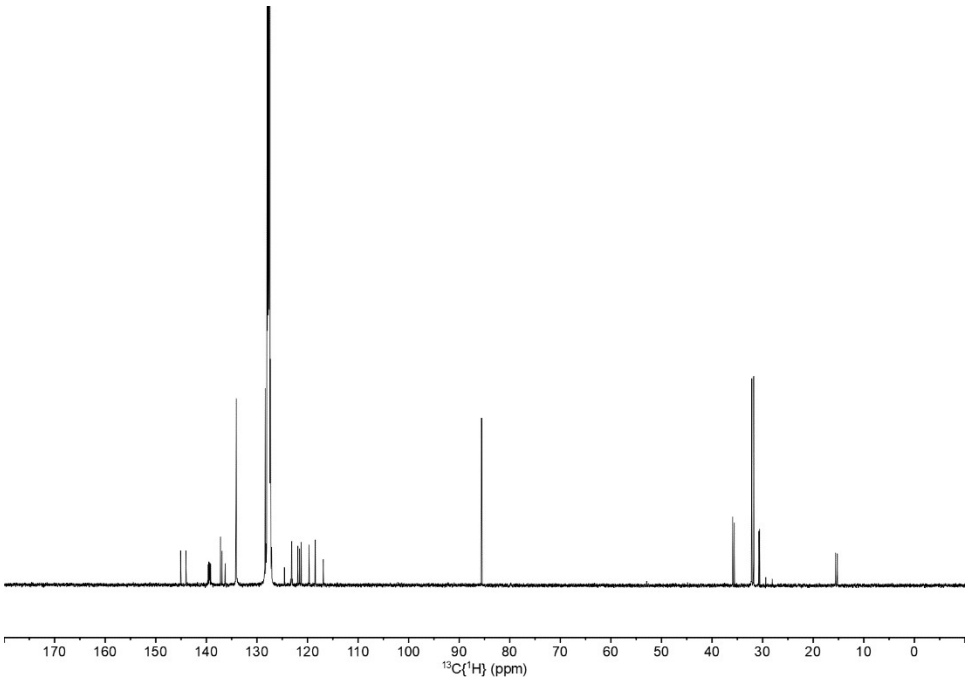

Figure S12 $^{13}C\{^{1}H\}$ NMR spectrum of **Ru2** (126 MHz, C_6D_6)

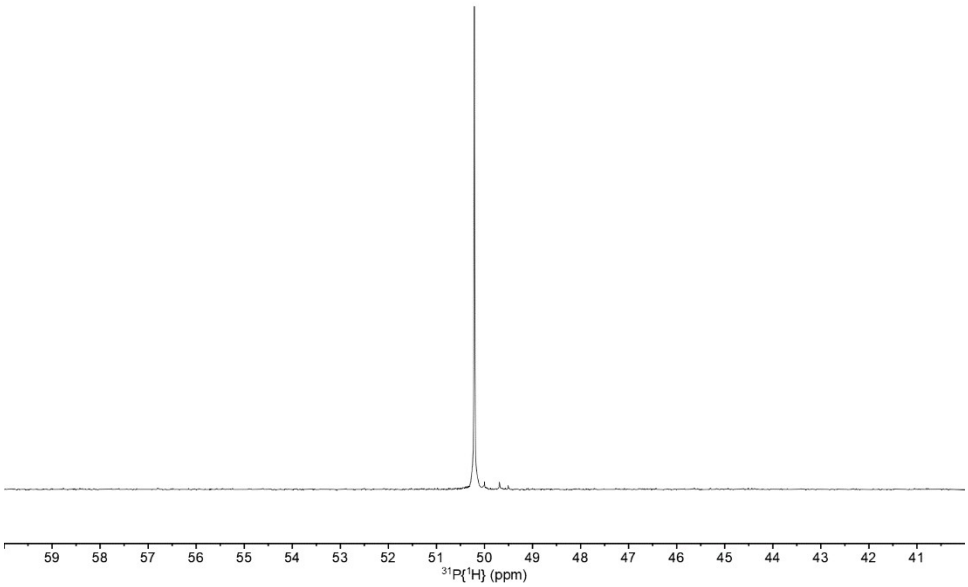

Figure S13 $^{31}P\{^{1}H\}$ NMR spectrum of **Ru2** (202 MHz, C_6D_6)

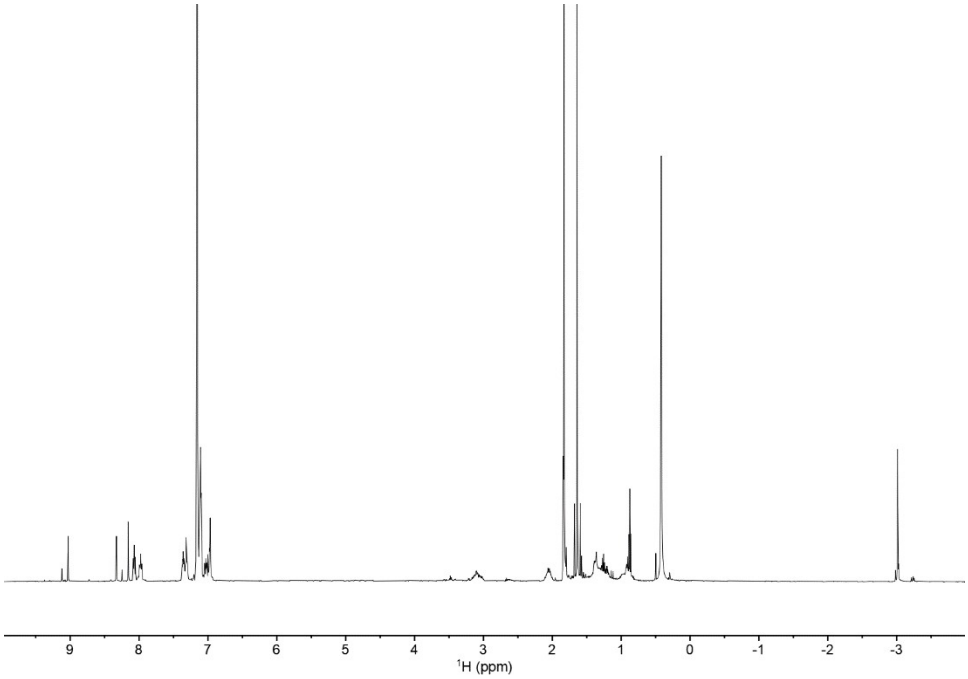

Figure S14 ^{1}H NMR spectrum full of **Ru4** (500 MHz, C_6D_6)

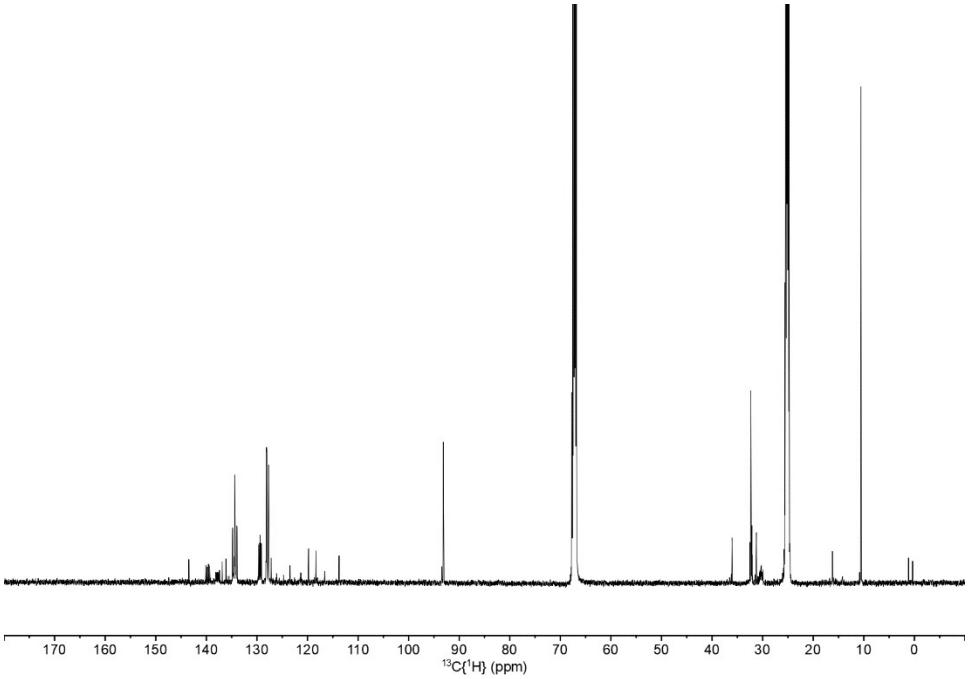

Figure S15 ^{13}C{^{1}H} NMR Full Spectrum of **Ru4** (126 MHz, THF-d8)

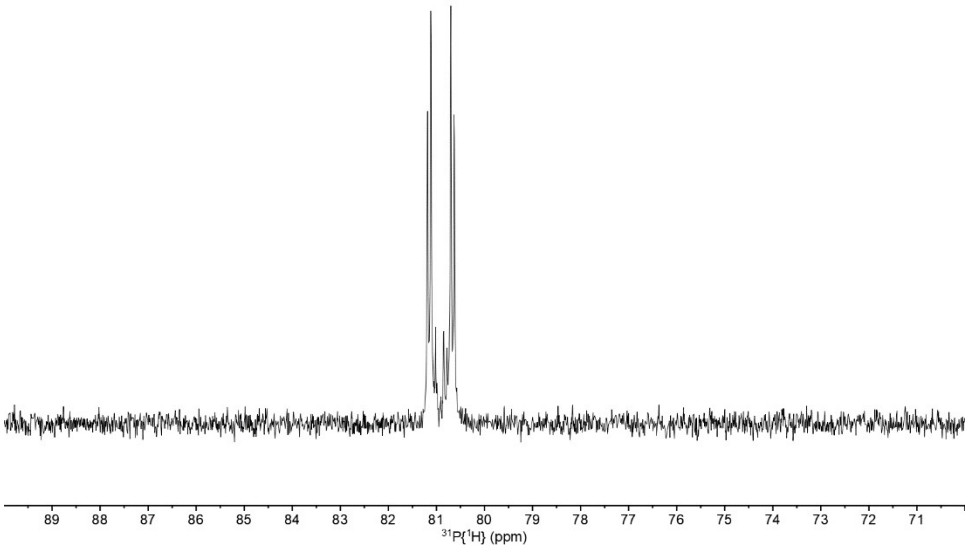

Figure S16 $^{31}P\{^{1}H\}$ NMR spectrum of **Ru4** (202 MHz, C_6D_6)

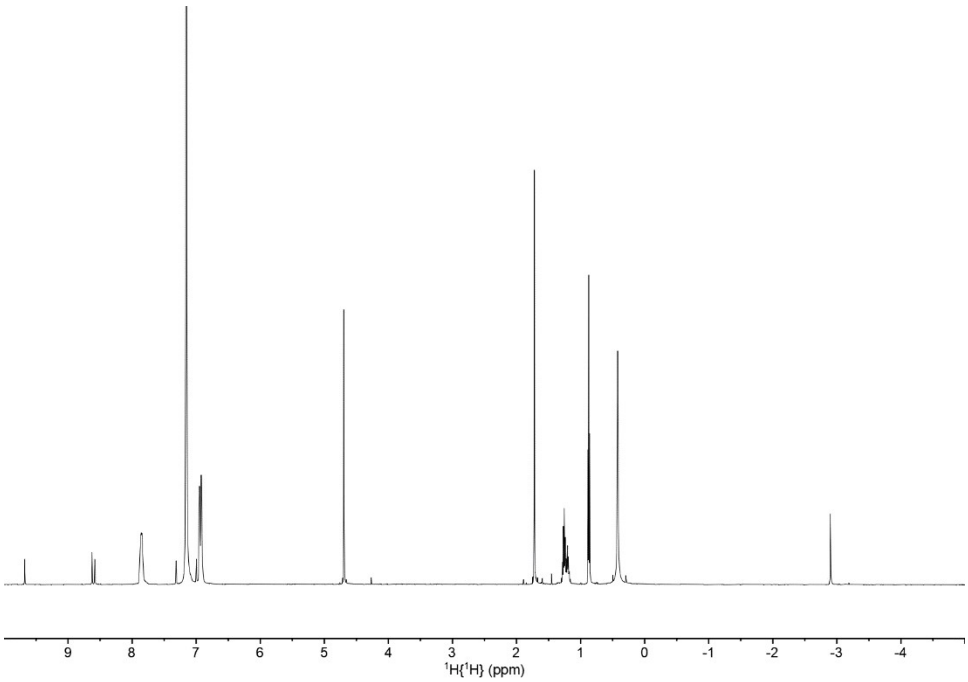

Figure S17 ^{1}H NMR full spectrum of **Ru5** (500 MHz, C_6D_6)

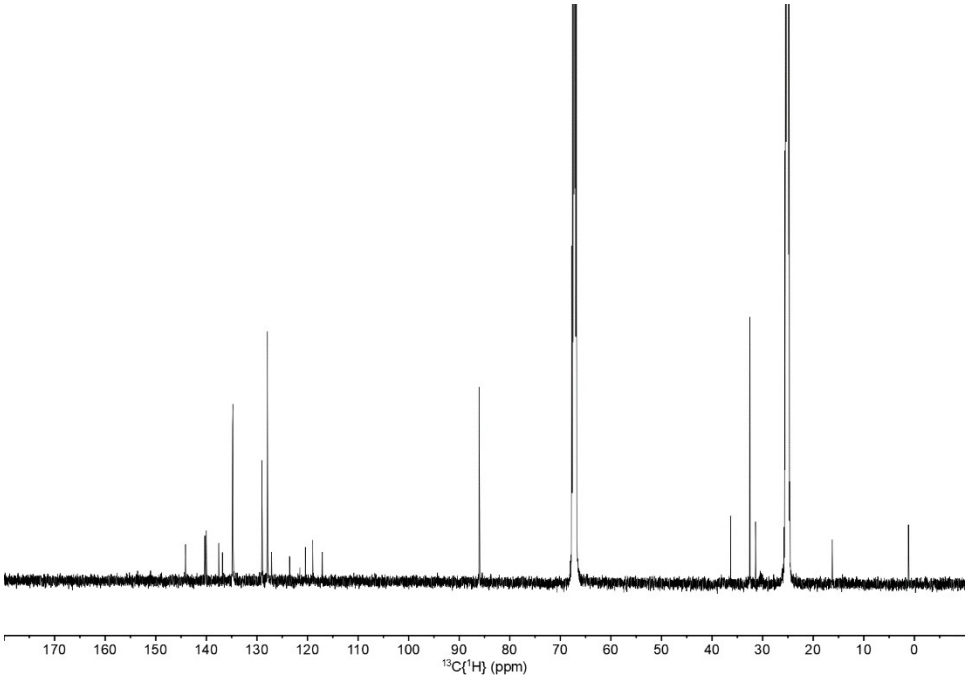

Figure S18 $^{13}C\{^{1}H\}$ NMR full spectrum of **Ru5** (126 MHz, THF-d8)

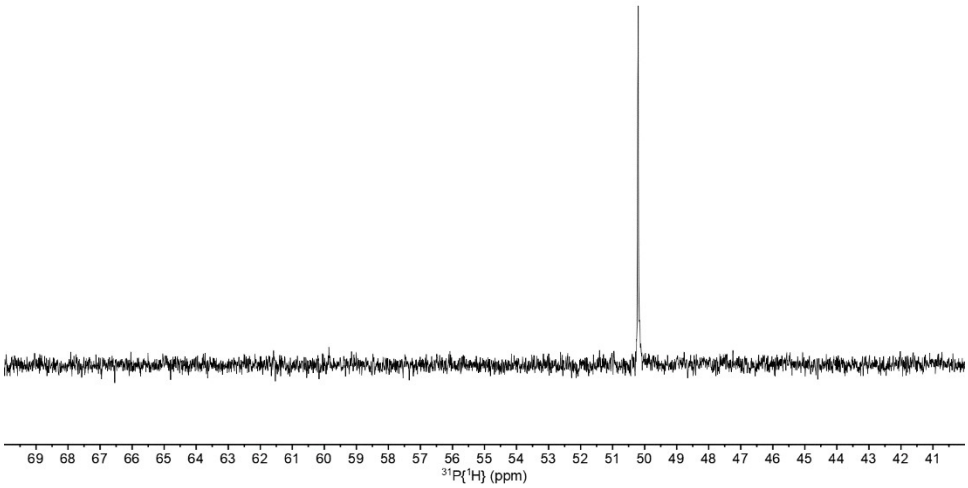

Figure S19 $^{31}P\{^{1}H\}$ NMR spectrum **Ru5** (202 MHz, C_6D_6)

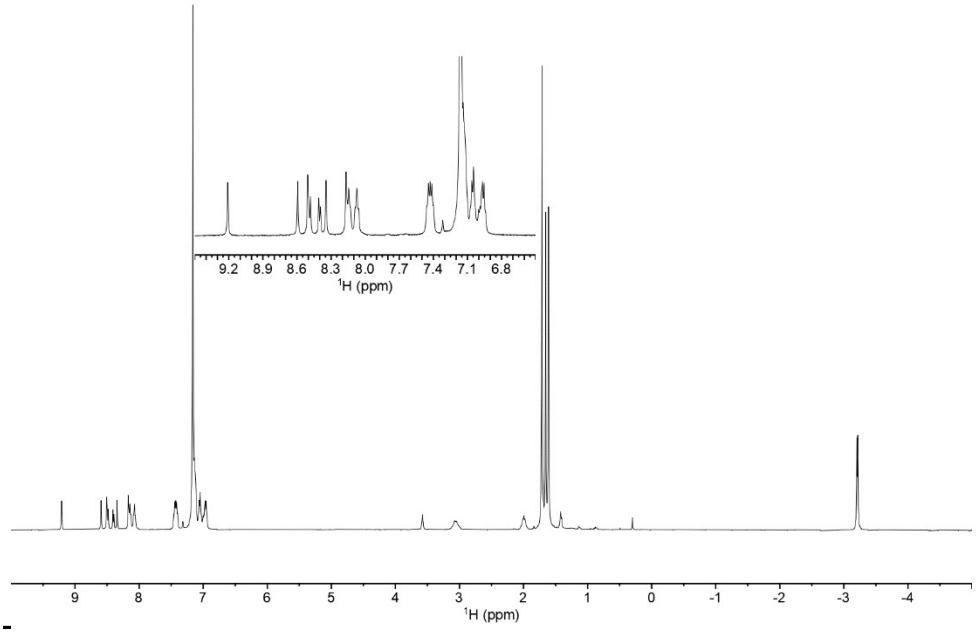

Figure S20 ^{1}H NMR full spectrum **Fe1** (500 MHz, C_6D_6)

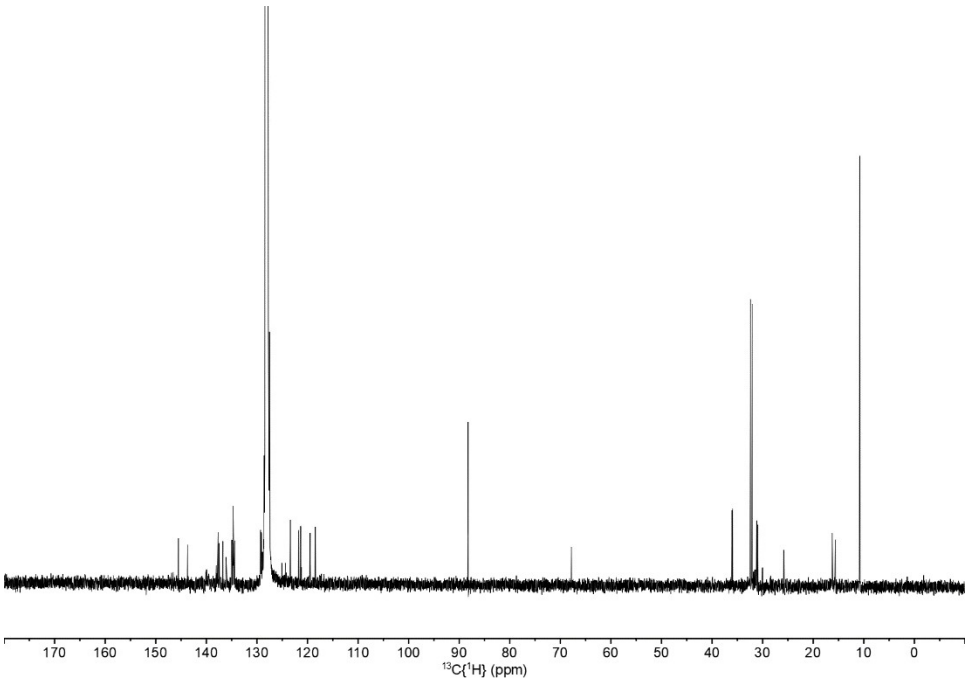

Figure S21 $^{13}C\{^{1}H\}$ NMR full spectrum **Fe1** (126 MHz, C_6D_6)

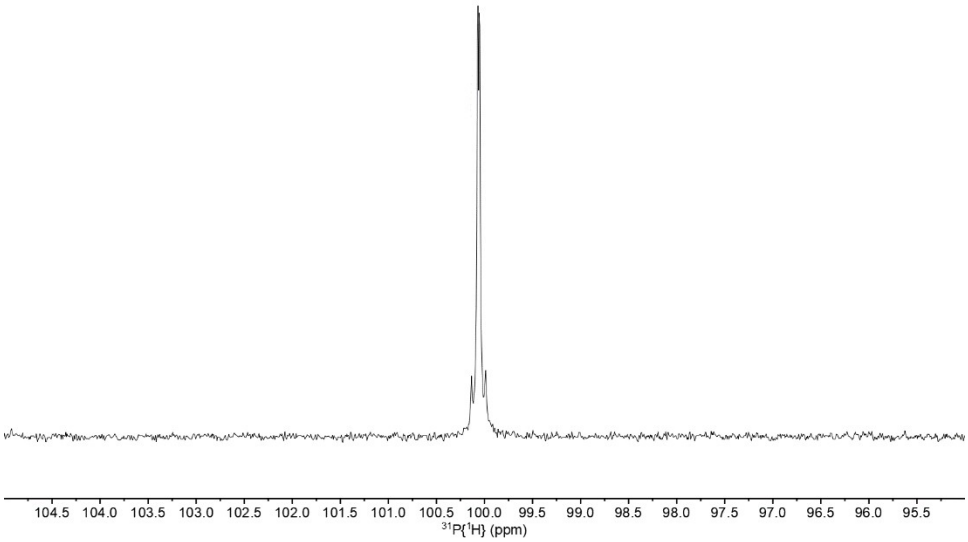

Figure S22 $^{31}P\{^{1}H\}$ NMR Spectrum **Fe1** (202 MHz, C_6D_6)

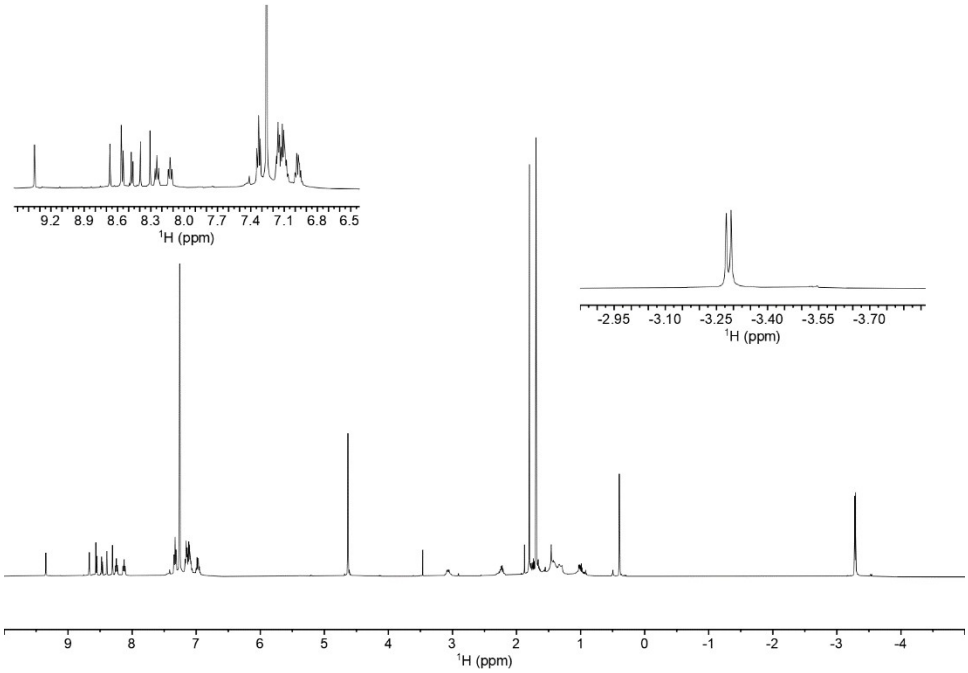

Figure S23 ^{1}H NMR Spectrum **Fe2** (500 MHz, C_6D_6)

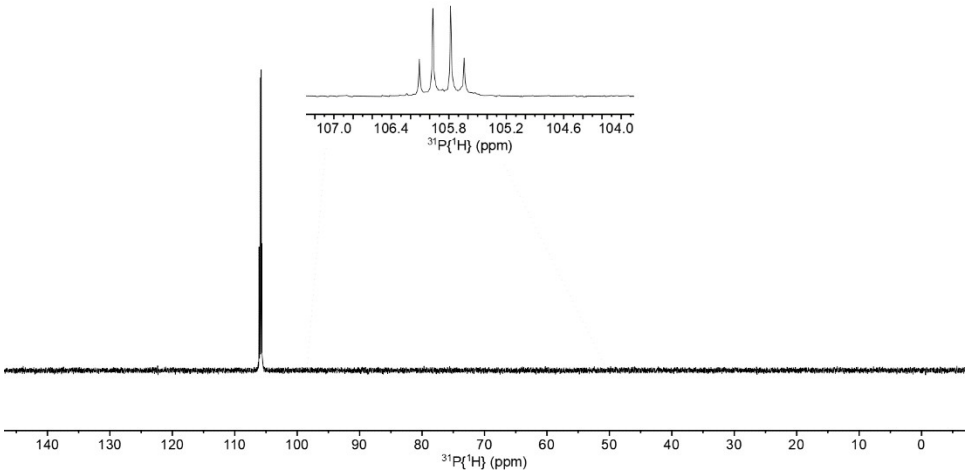

Figure S24 $^{31}P\{^{1}H\}$ NMR Spectrum **Fe2** (202 MHz, C_6D_6)

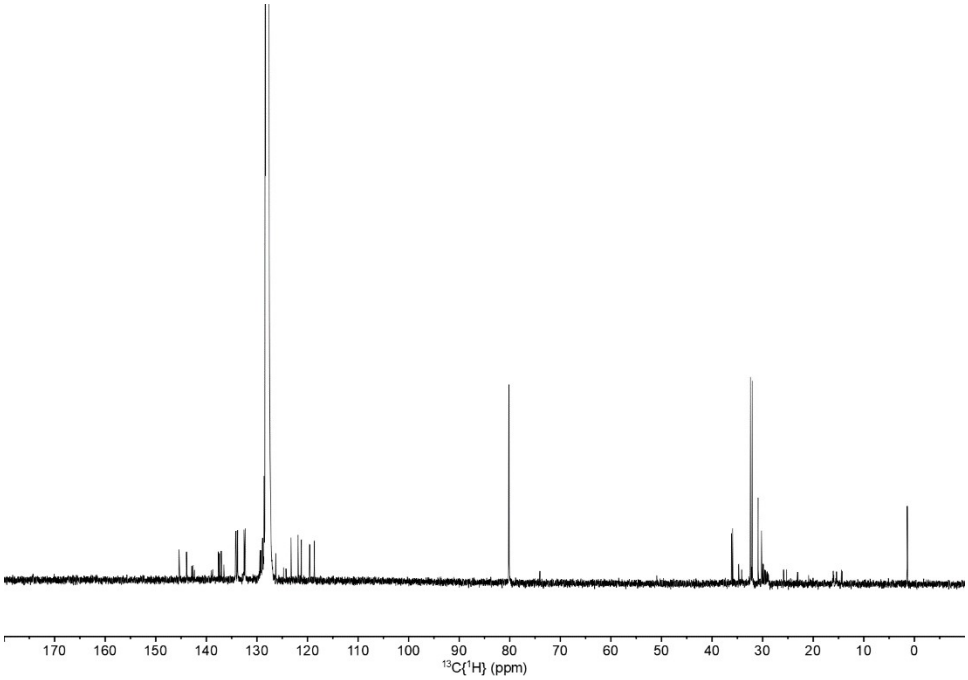

Figure S25 $^{13}C\{^{1}H\}$ NMR Spectrum **Fe2** (126 MHz, C_6D_6)

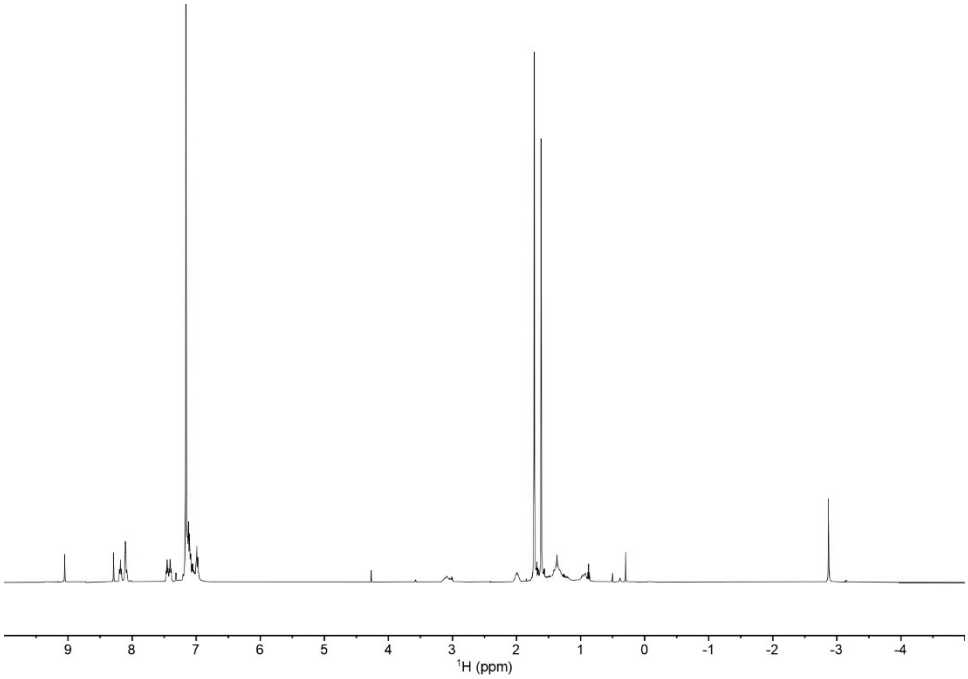

Figure S26 ^{1}H NMR full spectrum **Fe3** (500 MHz, C_6D_6)

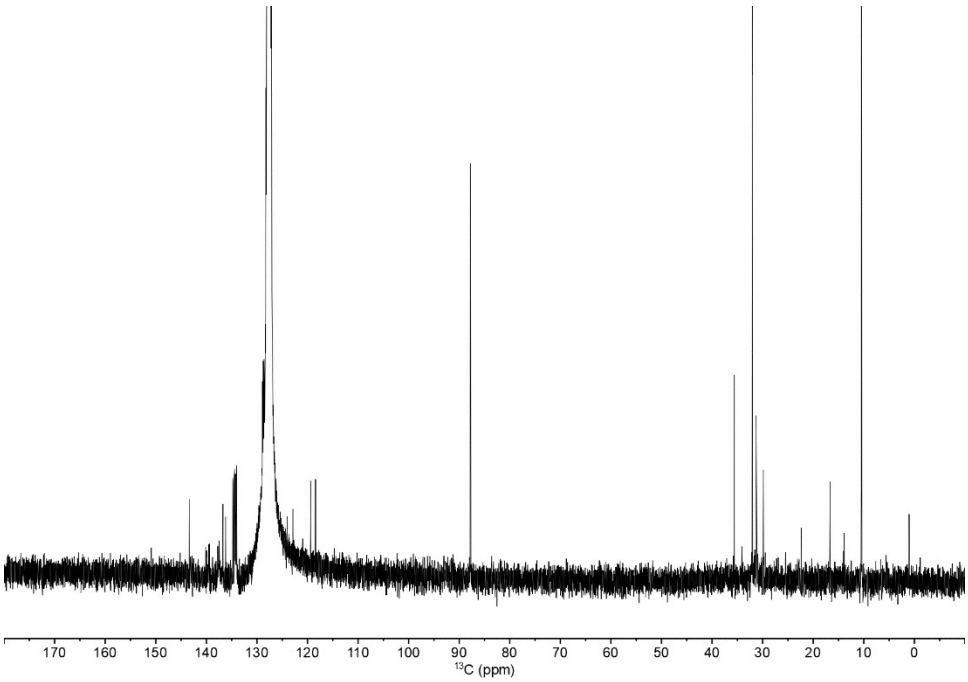

Figure S27 $^{13}C\{^{1}H\}$ NMR full spectrum Fe3 (126 MHz, C_6D_6)

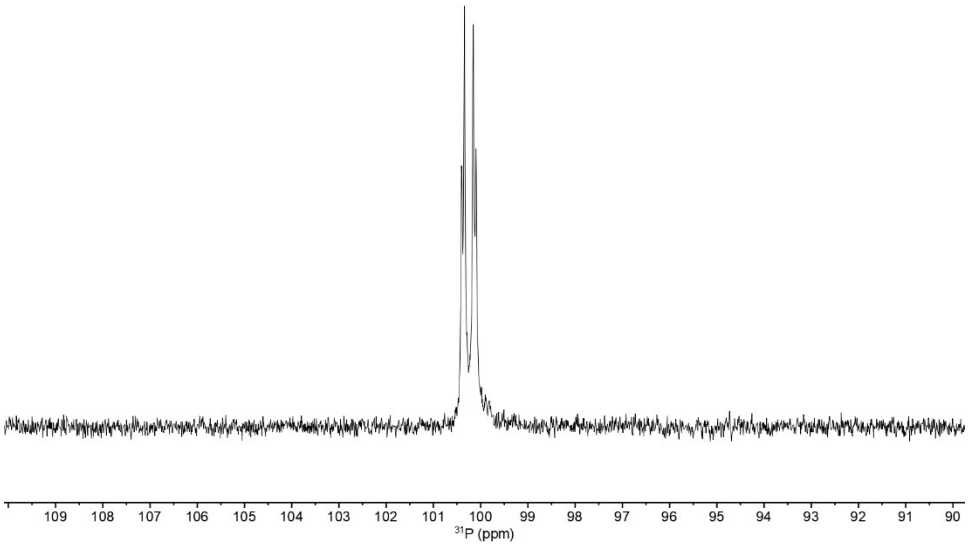

Figure S28 $^{31}P\{^{1}H\}$ NMR spectrum **Fe3** (202 MHz, C_6D_6)

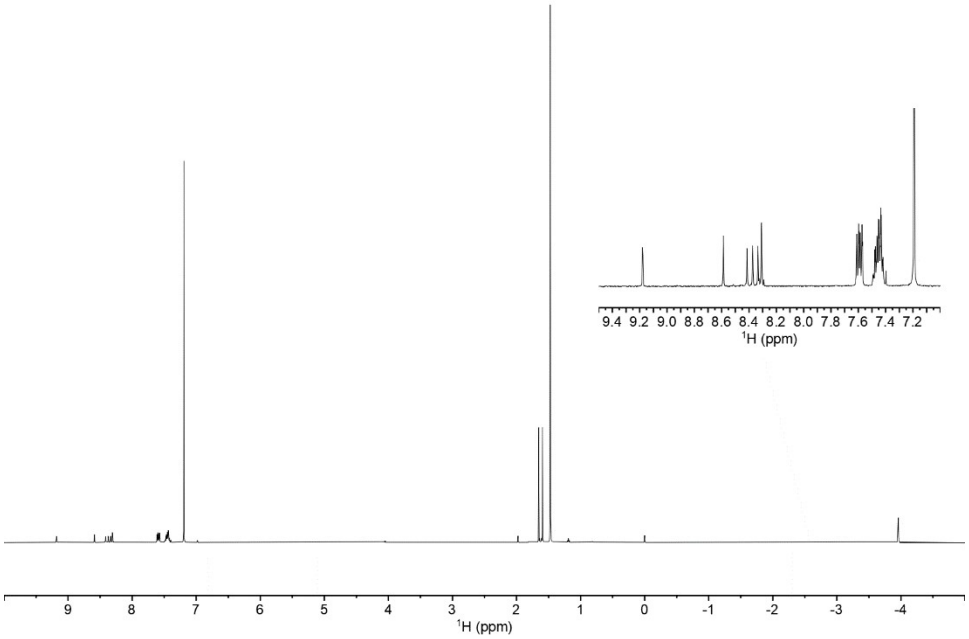

Figure S29 ^{1}H NMR spectrum **Au1** (500 MHz, $CDCl_3$)

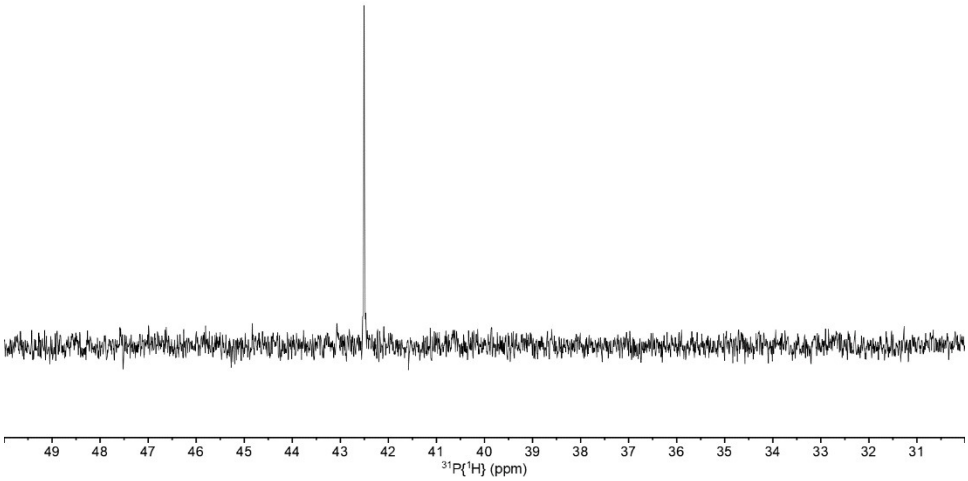

Figure S30 $^{31}P\{^{1}H\}$ NMR spectrum **Au1** (202 MHz, $CDCl_3$)

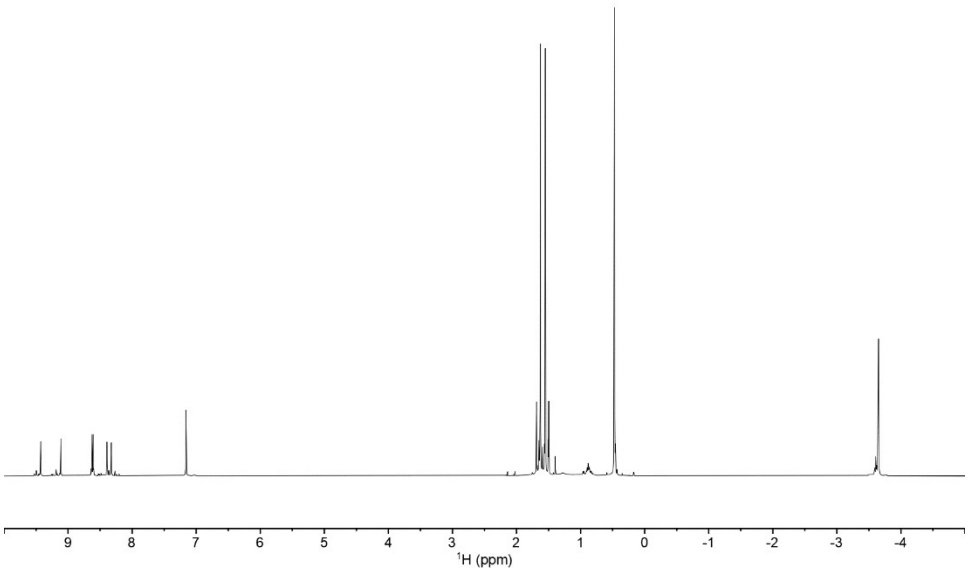

Figure S31 ^{1}H NMR spectrum **6** (500 MHz, C_6D_6)

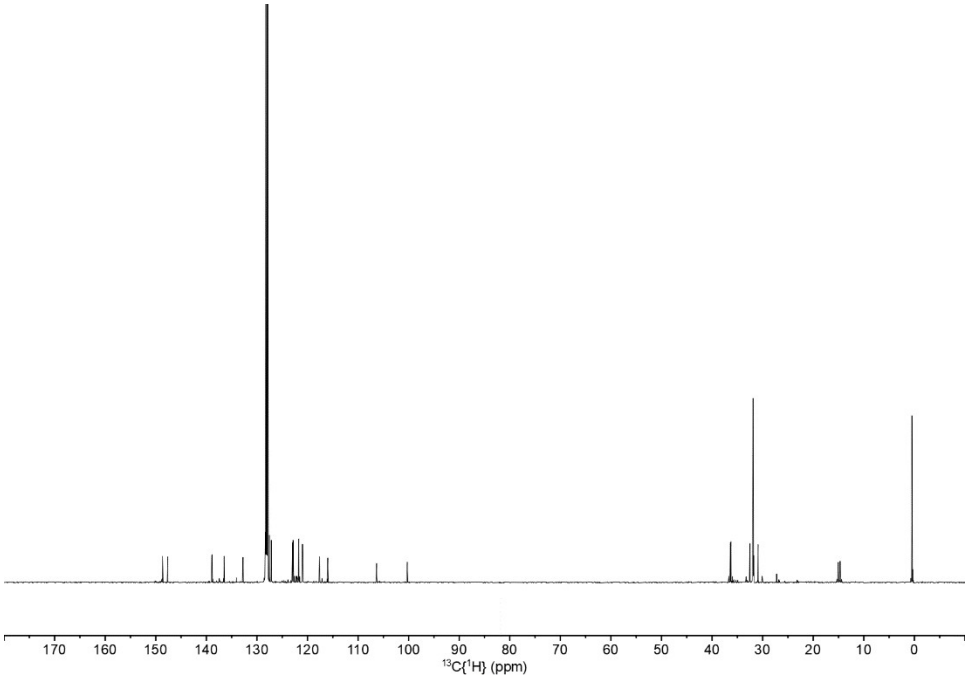

Figure S32 $^{13}C\{^{1}H\}$ NMR spectrum **6** (126 MHz, C_6D_6)

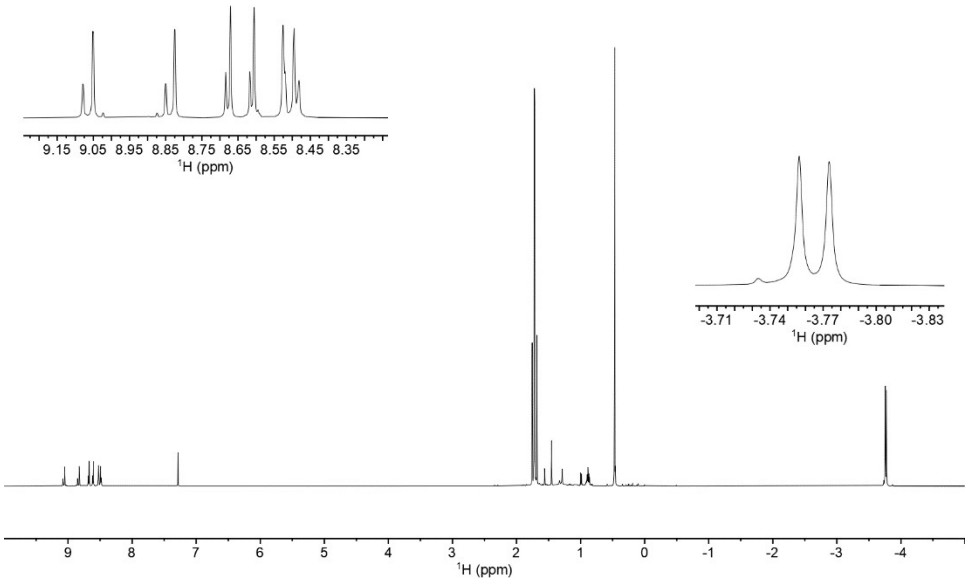

Figure S33 ^{1}H NMR spectrum **7** (500 MHz, $CDCl_3$)

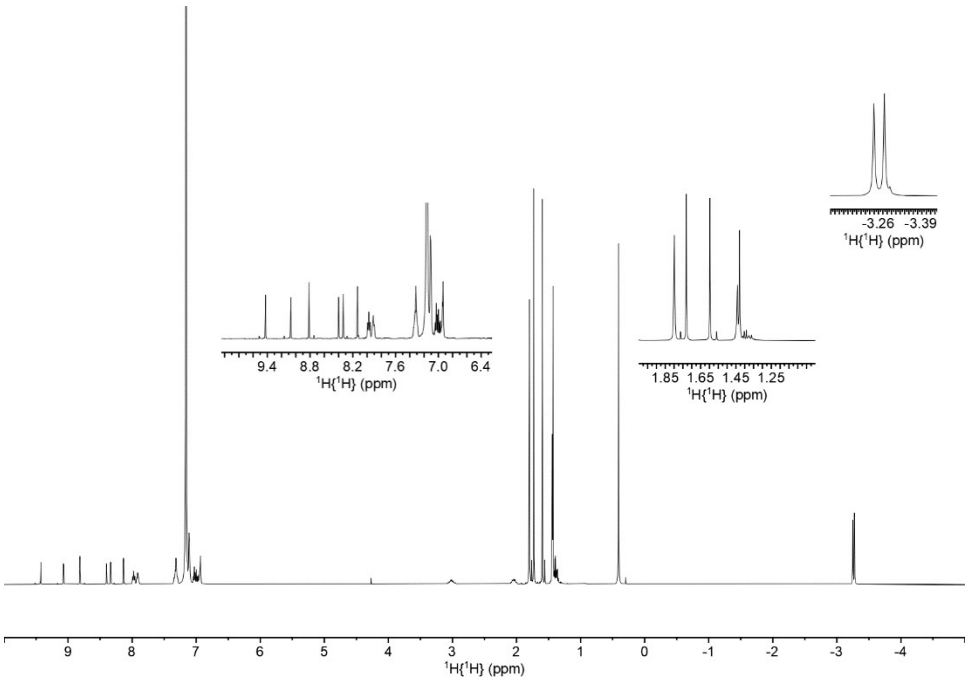

Figure S34 ^1H NMR spectrum **Ru6** (500 MHz, C_6D_6)

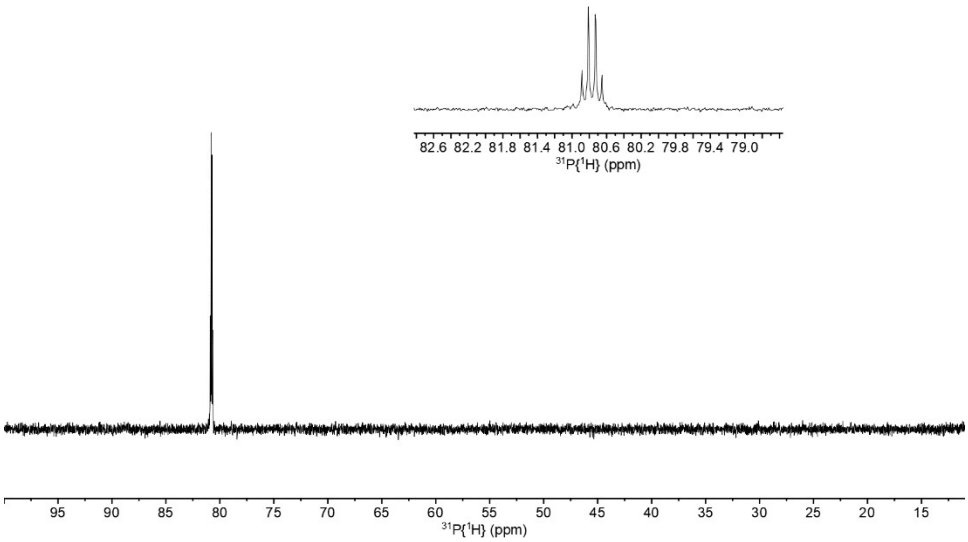

Figure S35 $^{31}P\{^1H\}$ NMR spectrum **Ru6** (202 MHz, C_6D_6)

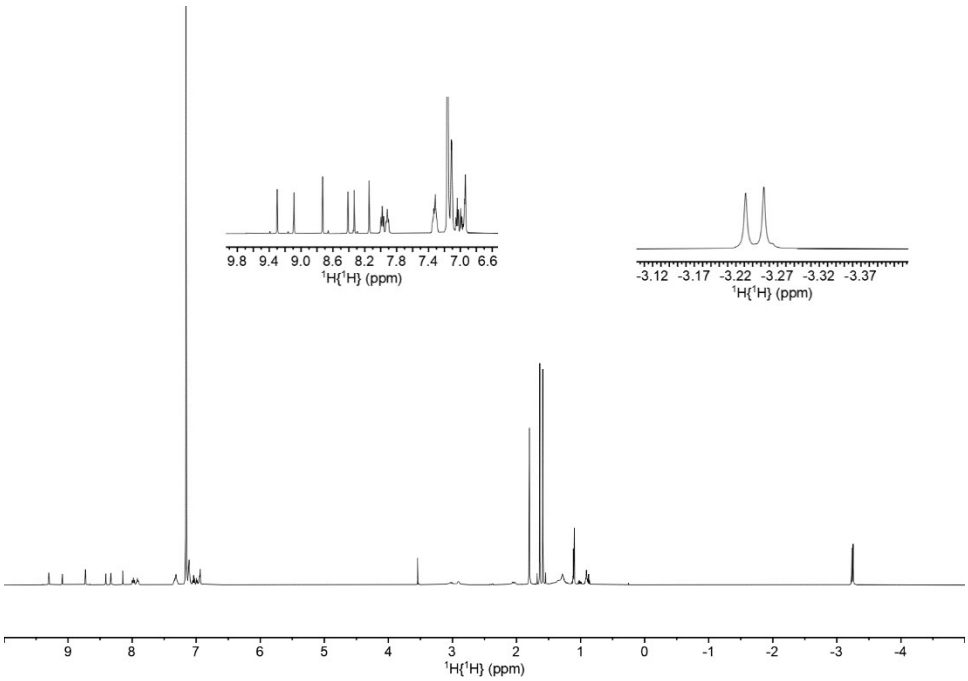

Figure S36 ^1H NMR spectrum **Ru7** (500 MHz, C_6D_6)

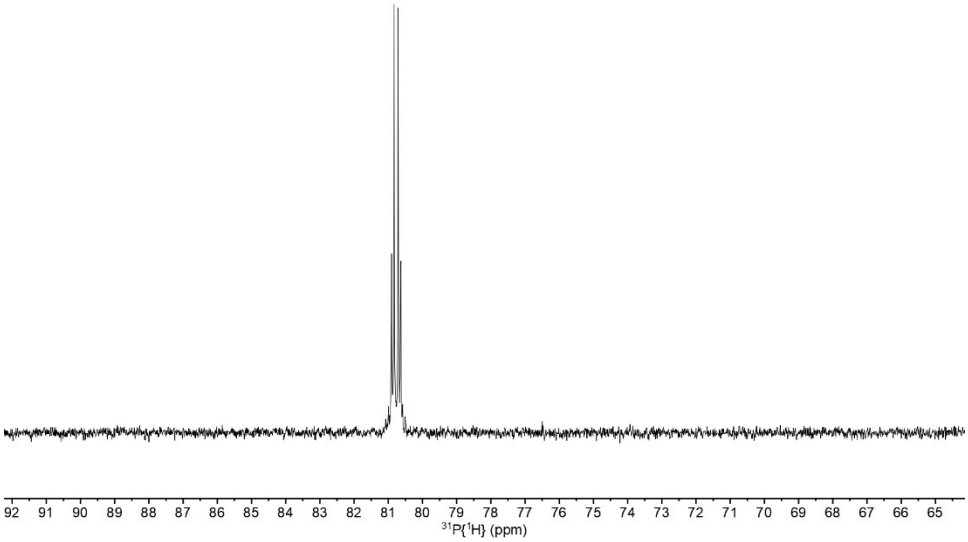

Figure S37 $^{31}P\{^1H\}$ NMR spectrum **Ru7** (202 MHz, C_6D_6)

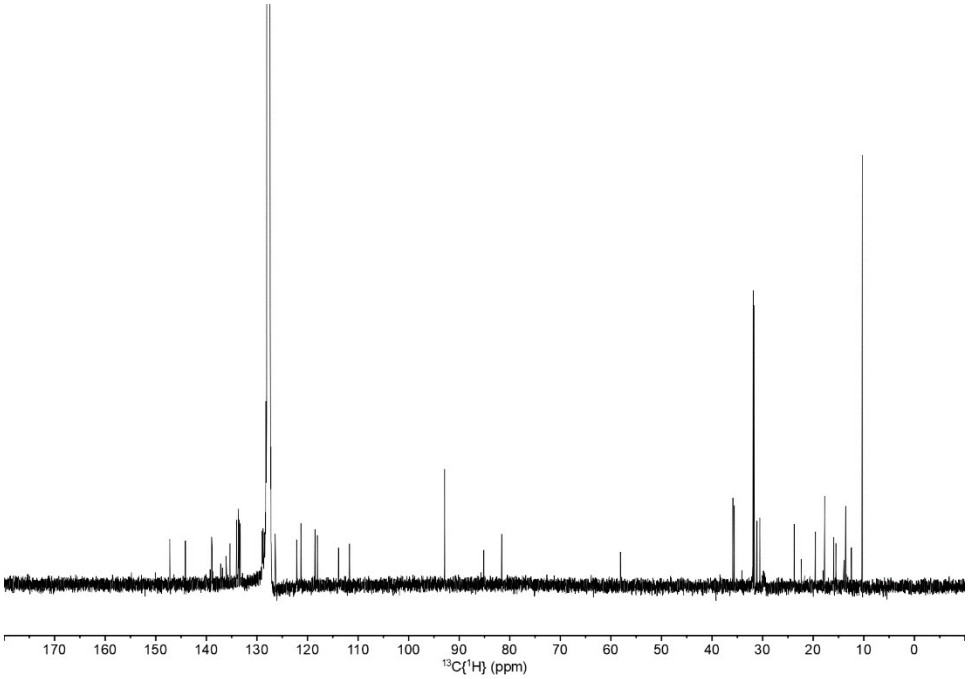

Figure S38 $^{13}C\{^{1}H\}$ NMR spectrum **Ru7** (202 MHz, C_6D_6)

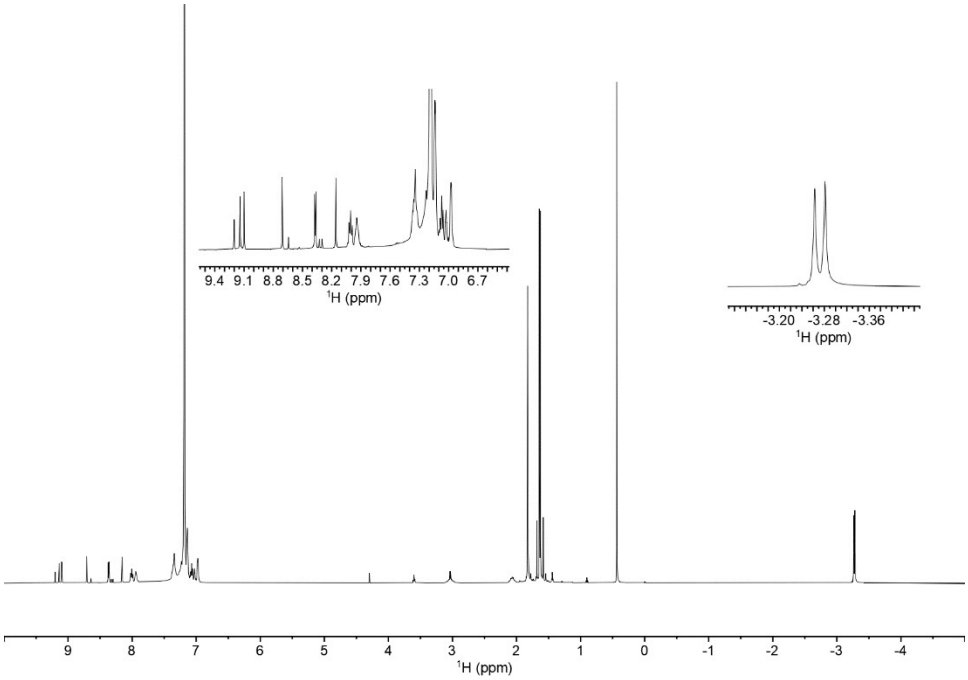

Figure S39 ^{1}H NMR spectrum **Ru8** (500 MHz, C_6D_6)

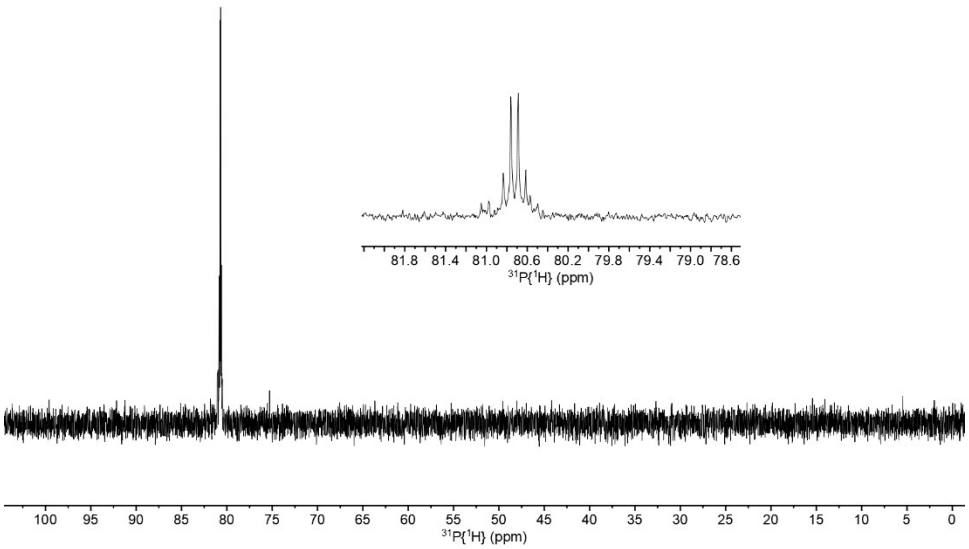

Figure S40 $^{31}P\{^{1}H\}$ NMR spectrum **Ru8** (C_6D_6)

UV-Vis Data

Table S1: Summary of UV-vis Absorption Data[a]

Complex	Wavelength (nm), (Molar Attenuation Coefficient ($L*mol^{-1} * cm^{-1}$))
Ru1	230 (49465), 257 (sh, 26732), 345 (37037), 435 (27869), 541 (13302), 685 (6868)
Ru2	231 (38159), 340 (21573), 425 (21700), 526 (6868), 677 (1478)
Ru4	230 (78025), 260 (sh, 40937), 335 (24774), 415 (sh, 25110), 440 (37714), 544 (sh, 14768), 586 (23114), 715 (12483)
Ru5	230 (77513), 323 (18557), 410 (sh, 22020), 435 (33124), 568 (15603), 705 (6893)
Fe1	231 (43619), 273 (sh, 17924), 350 (40584), 389 (21473), 458 (13707), 586 (11279), 642 (5598), 696 (3280)

[a]Samples were prepared in a glovebox and kept under inert conditions. The spectra were recorded in DCM with a quartz cell 1 cm path length. Concentrations were kept low so as not to exceed absorption > 1.

Crystallography

A suitable crystal was selected and mounted on a XtaLAB Synergy, single source diffractometer equipped with a HyPix detector, Oxford Diffraction Gemini-R Ultra, or Oxford Diffraction Xcalibur, Sapphire3. The crystal was kept at a steady temperature (T = 100 K) during data collection. Structure was solved with ShelXT 2018/2[1] structure solution program using dual methods and Olex2[2] as the graphical interface. Model refined using Xl (version 2018/3)[3] using least squared minimisation on F^2.

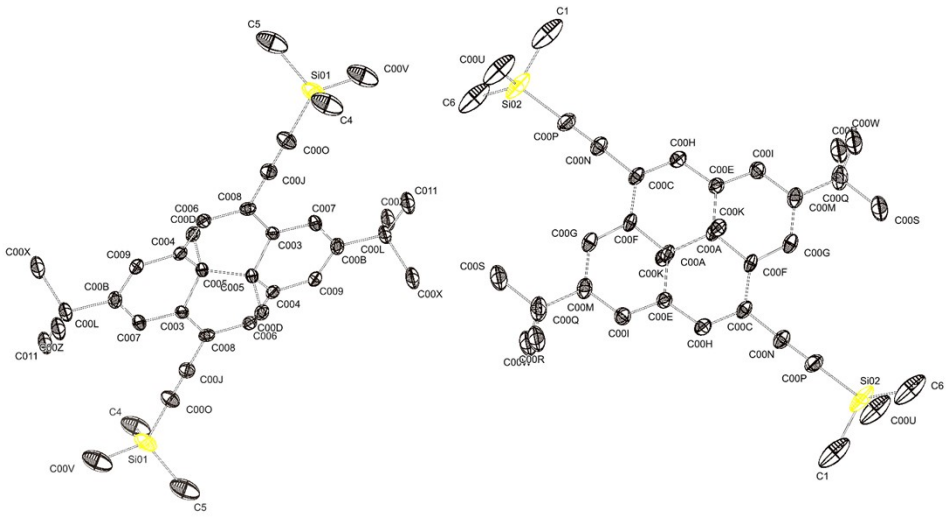

Figure S41 ORTEP representation of **3c**. Hydrogens removed for clarity. Atomic displacement ellipsoids drawn at 30 % probability. Disorder removed for clarity.

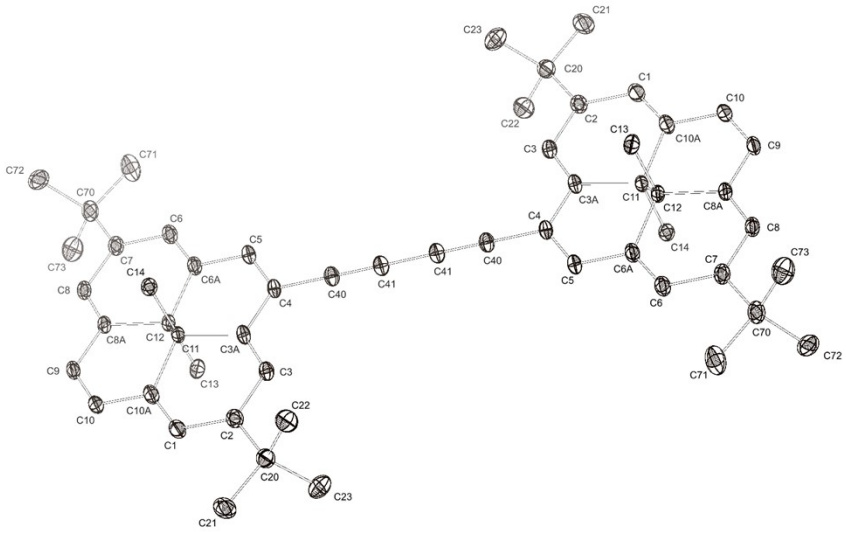

Figure S42 ORTEP representation of **5**. Hydrogens removed for clarity. Atomic displacement ellipsoids drawn at 30 % probability. Disorder removed for clarity.

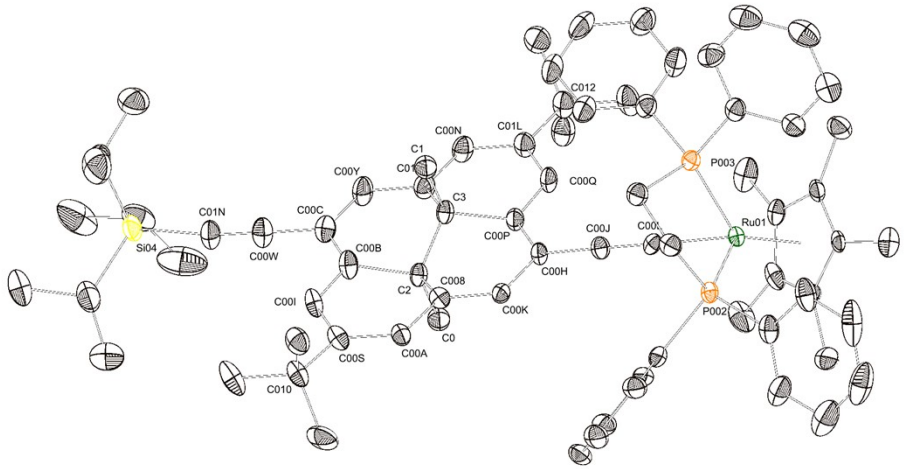

Figure S43 ORTEP representation of **Ru6**. Hydrogens removed for clarity. Atomic displacement ellipsoids drawn at 30 % probability. Disorder removed for clarity.

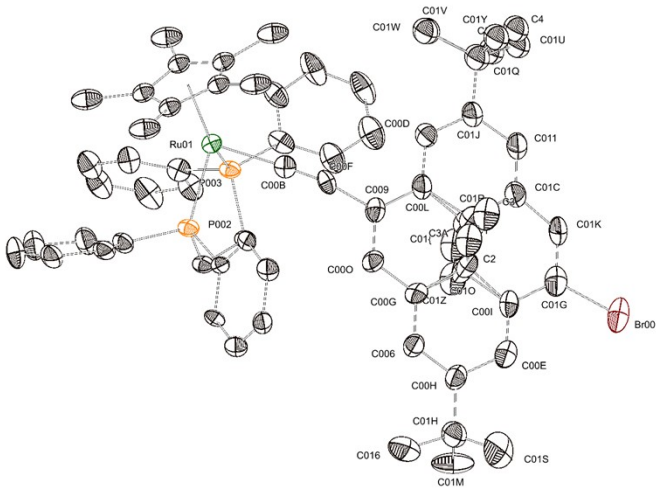

Figure S44 ORTEP representation of **Ru8**. Hydrogens removed for clarity. Atomic displacement ellipsoids drawn at 30 % probability. Disorder removed for clarity.

Table S2 Crystal data and structure refinement tables

Compound	**Ru1**	**Ru2**	**Ru2**	**3c**
Crystal data				
Chemical formula	$C_{64}H_{70}P_2Ru$	$C_{69}H_{66}P_2Ru·3(CH_2Cl_2)$	$C_{69}H_{66}P_2Ru$	$2(C_{18}H_{24}Si)$
M_r	1002.21	1313.00	1058.22	536.92
Crystal system, space group	Monoclinic, *I*2/*a*	Monoclinic, $P2_1/c$	Monoclinic, $P2_1/n$	Monoclinic, $P2_1/c$
a, *b*, *c* (Å)	28.3238 (2), 8.8378 (1), 44.5941 (3)	8.9102 (2), 15.2917 (4), 46.4839 (11)	11.8379 (2), 15.3879 (2), 29.6079 (5)	11.9812 (4), 21.0158 (5), 15.1892 (4)
β (°)	99.493 (1)	90.762 (2)	95.826 (1)	112.687 (4)
V (Å^3)	11009.93 (17)	6333.0 (3)	5365.53 (15)	3528.6 (2)
Z	8	4	4	4
Radiation type	Cu *K*α	Mo *K*α	Mo *K*α	Cu *K*α
μ (mm^{-1})	3.13	0.59	0.40	1.04
Crystal size (mm)	0.23 × 0.09 × 0.06	0.23 × 0.21 × 0.10	0.36 × 0.28 × 0.20	0.09 × 0.08 × 0.07
Data collection				
Diffractometer	XtaLAB Synergy, Single source, HyPix	Oxford Diffraction Xcalibur, Sapphire3 CCD	Oxford Diffraction Xcalibur, Sapphire3 CCD	XtaLAB Synergy, Single source, HyPix
Absorption correction	Gaussian *CrysAlis PRO* 1.171.43.70a (Rigaku Oxford Diffraction, 2023) Empirical absorption correction using spherical harmonics, implemented in SCALE3 ABSPACK scaling algorithm.	Multi-scan *CrysAlis PRO* 1.171.38.46 (Rigaku Oxford Diffraction, 2015) Empirical absorption correction using spherical harmonics, implemented in SCALE3 ABSPACK scaling algorithm.	Multi-scan *CrysAlis PRO* 1.171.38.46 (Rigaku Oxford Diffraction, 2015) Empirical absorption correction using spherical harmonics, implemented in SCALE3 ABSPACK scaling algorithm.	Gaussian *CrysAlis PRO* 1.171.41.103a (Rigaku Oxford Diffraction, 2021) Empirical absorption correction using spherical harmonics, implemented in SCALE3 ABSPACK scaling algorithm.
T_{min}, T_{max}	0.621, 1.000	0.959, 1.0	0.849, 1.0	0.310, 1.000
$(\sin\theta/\lambda)_{max}$ (Å^{-1})	0.628	0.741	0.747	0.625
Refinement				
$R[F^2 > 2\sigma(F^2)]$, $wR(F^2)$, *S*	0.035, 0.093, 1.09	0.124, 0.346, 1.01	0.049, 0.130, 1.00	0.124, 0.279, 1.15
No. of reflections	11004	20731	17844	6014
No. of parameters	635	752	725	362
No. of restraints	11	18	12	70
	$w = 1/[\sigma^2(F_o^2) + (0.0421P)^2 + 24.8448P]$ where $P = (F_o^2 + 2F_c^2)/3$	$w = 1/[\sigma^2(F_o^2) + (0.140P)^2 + 65.P]$ where $P = (F_o^2 + 2F_c^2)/3$	$w = 1/[\sigma^2(F_o^2) + (0.060P)^2 + 5.P]$ where $P = (F_o^2 + 2F_c^2)/3$	$w = 1/[\sigma^2(F_o^2) + (0.0884P)^2 + 9.9808P]$ where $P = (F_o^2 + 2F_c^2)/3$
$\Delta\rho_{max}$, $\Delta\rho_{min}$ (e Å^{-3})	0.61, -1.04	2.83, -1.98	2.06, -1.69	0.66, -0.64

Computer programs: CrysAlis PRO system (CCD 41.104a 64-bit (release 16-03-2021)), CrysAlis PRO 1.171.38.46 (Rigaku OD, 2015), CrysAlis PRO 1.171.43.70a (Rigaku OD, 2023), XT (Sheldrick, 2015), SHELXT 2018/2 (Sheldrick, 2018), SHELXT2015/1 (Sheldrick, 2015), XL (Sheldrick, 2008), SHELXL2017/1 (Sheldrick, 2017), Olex2 1.5 (Dolomanov et al., 2009).

Table S3 Crystal data and structure refinement tables

Compound	**5**	**Ru6**	**Ru8**
Crystal data			
Chemical formula	$C_{56}H_{62}$	C75H90P2RuSi (CH_2Cl_2)	$C_{64}H_{69}BrP_2Ru$
M_r	735.06	1267.50	1081.10
Crystal system, space group	Monoclinic, $P2_1/n$	Orthombic, $P2_12_12$	Orthombic, $Pna2_1$
a, b, c (Å)	9.6557 (2), 12.9547 (2), 18.6848 (3)	28.0052 (2), 27.3628 (2), 8.7392 (1)	31.4242 (14), 19.2612 (9), 8.9346 (7)
β (°)	101.938 (1)	90	90
V (Å^3)	2286.67 (7)	6696.86 (10)	5407.8 (5)
Z	2	4	4
Radiation type	Mo $K\alpha$	Cu $K\alpha$	Cu $K\alpha$
μ (mm^{-1})	0.060	3.560	4.058
Crystal size (mm)	0.402 × 0.284 × 0.197	0.09 × 0.06 × 0.05	0.07 × 0.03 × 0.01
Data collection			
Diffractometer	Oxford Diffraction Gemini-R Ultra	XtaLAB Synergy, Single source, HyPix	XtaLAB Synergy, Single source, HyPix
Absorption correction	Multi-scan *CrysAlis PRO* 1.171.39.46 (Rigaku Oxford Diffraction, 2015) Empirical absorption correction using spherical harmonics, implemented in SCALE3 ABSPACK scaling algorithm.	Gaussian *CrysAlis PRO* 1.171.41.103a (Rigaku Oxford Diffraction, 2021) Empirical absorption correction using spherical harmonics, implemented in SCALE3 ABSPACK scaling algorithm.	Gaussian *CrysAlis PRO* 1.171.41.103a (Rigaku Oxford Diffraction, 2021) Empirical absorption correction using spherical harmonics, implemented in SCALE3 ABSPACK scaling algorithm.
T_{min}, T_{max}	0.980, 0.988	0.774, 0.837	0.803, 0.907
$(\sin\theta/\lambda)_{max}$ (Å^{-1})	0.761	0.628	0.595
Refinement			
$R[F^2 > 2\sigma(F^2)]$, $wR(F^2)$, S	0.0547, 0.1229, 1.002	0.0410, 0.0901, 1.043	0.1110, 0.2049, 1.136
No. of reflections	8016	13538	8865
No. of parameters	300	761	557
No. of restraints	0	7	296
$\Delta\rho_{max}$, $\Delta\rho_{min}$ (e Å^{-3})	0.710, -0.169	1.002, -0.855	1.710, -1.681

Computer programs: CrysAlis PRO system (CCD 41.104a 64-bit (release 16-03-2021)), CrysAlis PRO 1.171.38.46 (Rigaku OD, 2015), CrysAlis PRO 1.171.43.70a (Rigaku OD, 2023), XT (Sheldrick, 2015), SHELXT 2018/2 (Sheldrick, 2018), SHELXT2015/1 (Sheldrick, 2015), XL (Sheldrick, 2008), SHELXL2017/1 (Sheldrick, 2017), Olex2 1.5 (Dolomanov et al., 2009).

Electrochemistry

a

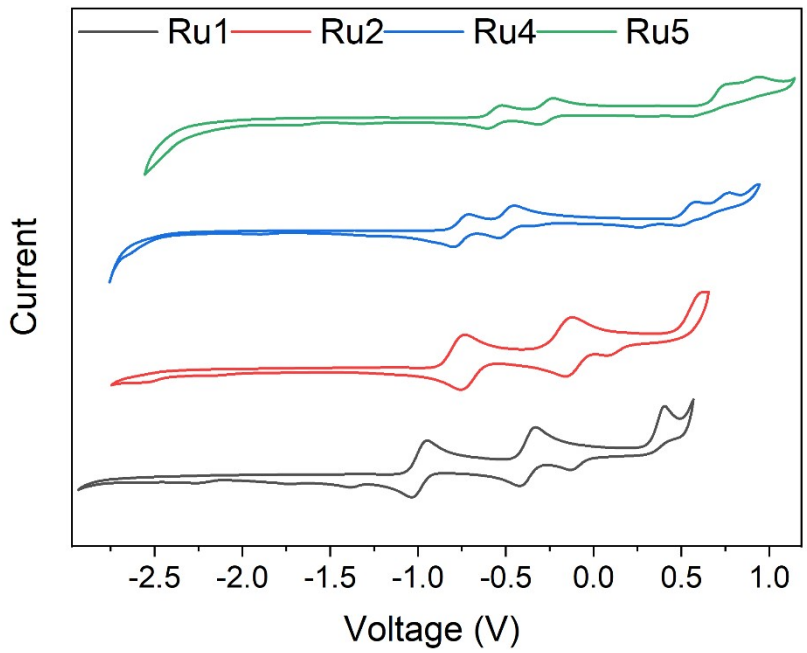

b

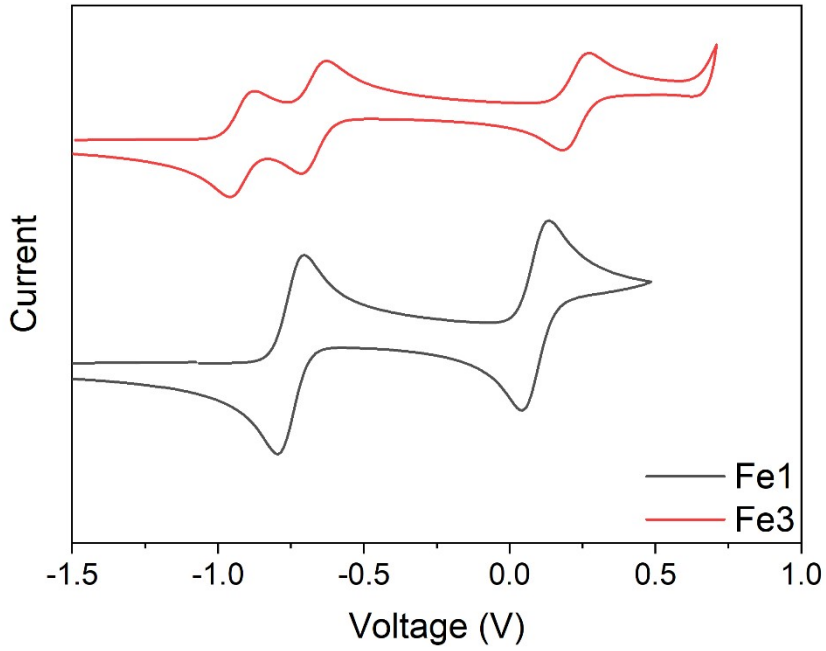

Figure S43 Collected cyclic voltammograms (IUPAC convention) for **Ru1,2,4,5** (a) and **Fe1,3** (b) complexes. Voltammetry experiments were carried out in a three-electrode cell using a Pt disc working electrode and Pt coated Ti rods as counter and pseudo-reference electrodes in 0.1 M Bu_4NPF_6 / CH_2Cl_2 solutions at ambient temperature. No correction for IR compensation was employed.

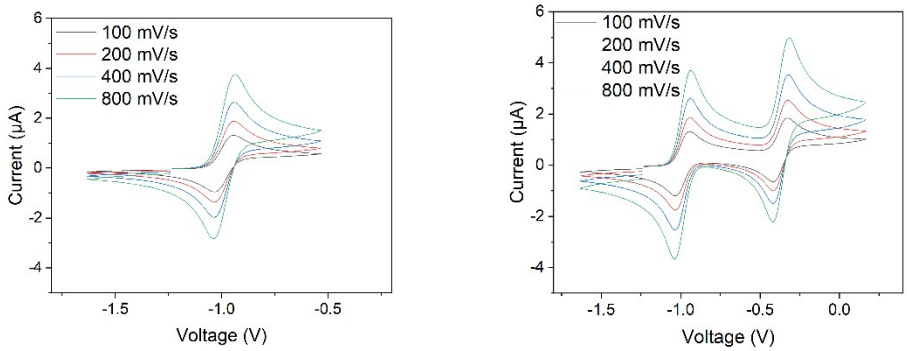

Figure S44 Cyclic voltammograms (IUPAC convention) for **Ru1**. Voltammetry experiments were carried out in a three-electrode cell using a Pt disc working electrode and Pt coated Ti rods as counter and pseudo-reference electrodes in 0.1 M Bu_4NPF_6 / CH_2Cl_2 solutions at ambient temperature. No correction for IR compensation was employed.

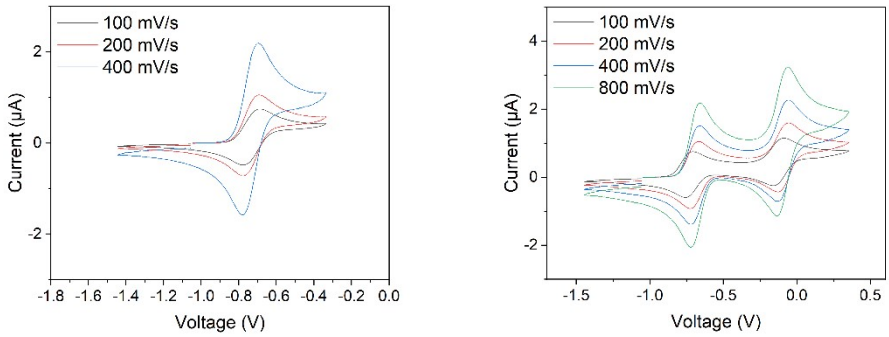

Figure S45 Cyclic voltammograms (IUPAC convention) for **Ru2**. Voltammetry experiments were carried out in a three-electrode cell using a Pt disc working electrode and Pt coated Ti rods as counter and pseudo-reference electrodes in 0.1 M Bu_4NPF_6 / CH_2Cl_2 solutions at ambient temperature. No correction for IR compensation was employed.

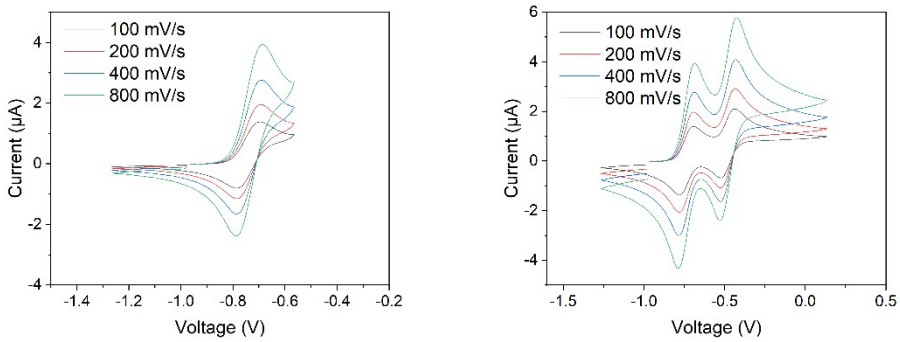

Figure S46 Cyclic voltammograms (IUPAC convention) for **Ru4**. Voltammetry experiments were carried out in a three-electrode cell using a Pt disc working electrode and Pt coated Ti rods as counter and pseudo-reference electrodes in 0.1 M Bu_4NPF_6 / CH_2Cl_2 solutions at ambient temperature. No correction for IR compensation was employed.

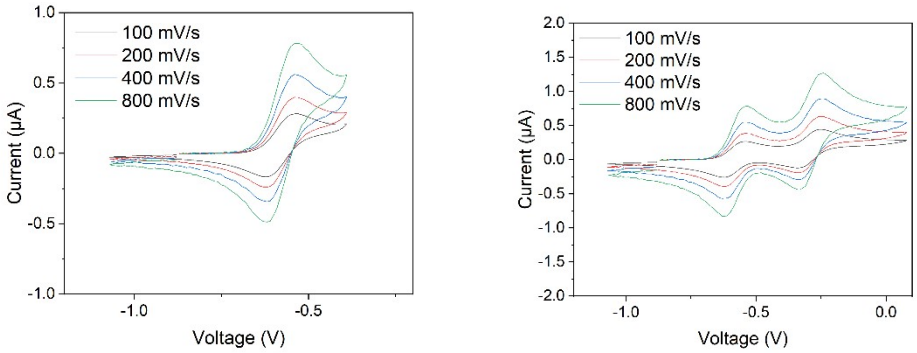

Figure S47 Cyclic voltammograms (IUPAC convention) for **Ru5**. Voltammetry experiments were carried out in a three-electrode cell using a Pt disc working electrode and Pt coated Ti rods as counter and pseudo-reference electrodes in 0.1 M Bu_4NPF_6 / CH_2Cl_2 solutions at ambient temperature. No correction for IR compensation was employed.

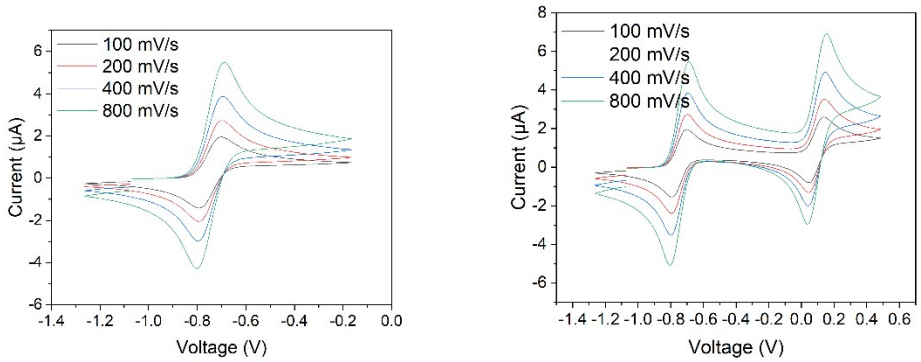

Figure S48 Cyclic voltammograms (IUPAC convention) for **Fe1**. Voltammetry experiments were carried out in a three-electrode cell using a Pt disc working electrode and Pt coated Ti rods as counter and pseudo-reference electrodes in 0.1 M Bu_4NPF_6 / CH_2Cl_2 solutions at ambient temperature. No correction for IR compensation was employed.

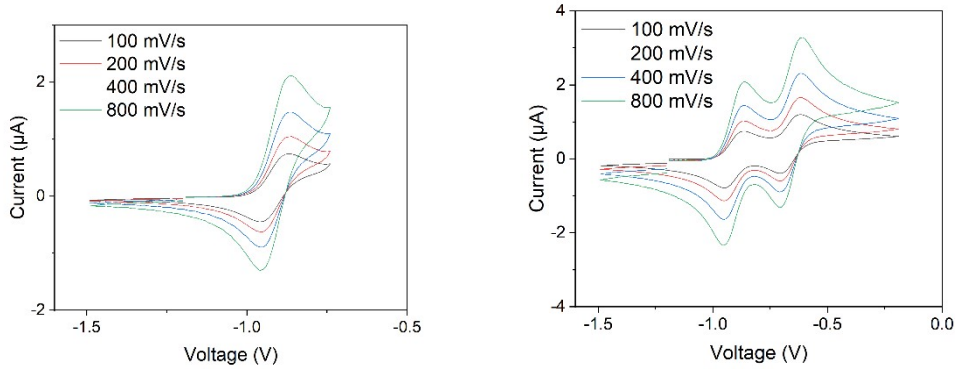

Figure S49 Cyclic voltammograms (IUPAC convention) for **Fe3**. Voltammetry experiments were carried out in a three-electrode cell using a Pt disc working electrode and Pt coated Ti rods as counter and pseudo-reference electrodes in 0.1 M Bu_4NPF_6 / CH_2Cl_2 solutions at ambient temperature. No correction for IR compensation was employed.

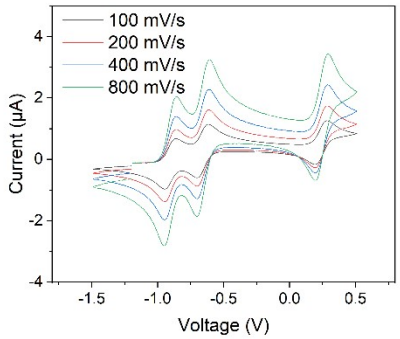

Figure S50 Cyclic voltammogram (IUPAC convention) for **Fe3**. Voltammetry experiments were carried out in a three-electrode cell using a Pt disc working electrode and Pt coated Ti rods as counter and pseudo-reference electrodes in 0.1 M Bu_4NPF_6 / CH_2Cl_2 solutions at ambient temperature. No correction for IR compensation was employed.

Irradiation Experiments

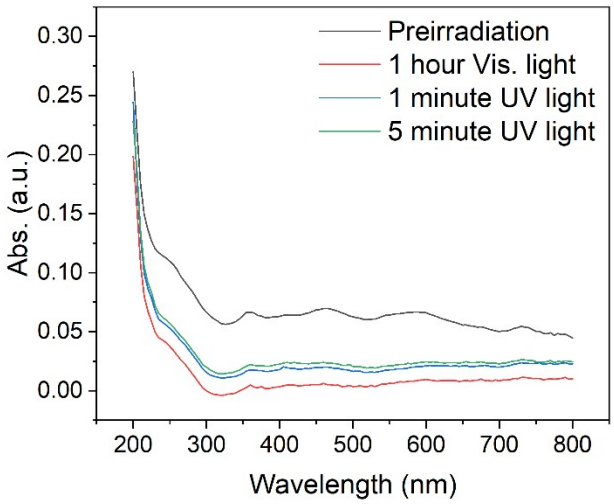

Figure S51 UV-vis spectra for **Fe3** after irradiation with visible and UV light

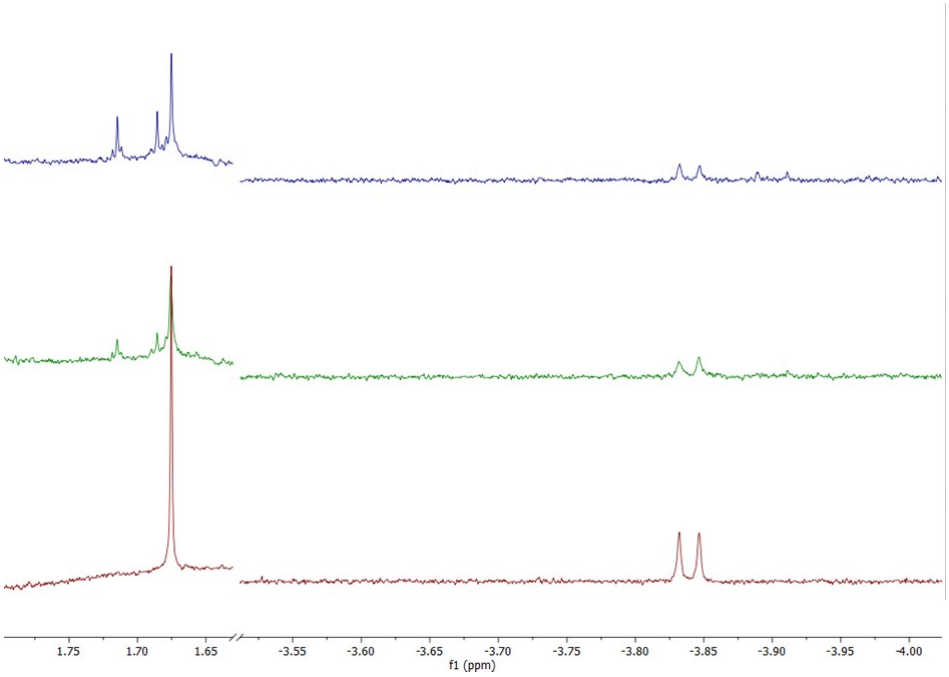

Figure S52 Changing NMR spectra of **Ru2** upon irradiation overnight. Red is pre-irradiation , green is after 3 hours irradiation with visible light and blue is after irradiation overnight (17 h) with visible light.

Spectroelectrochemistry

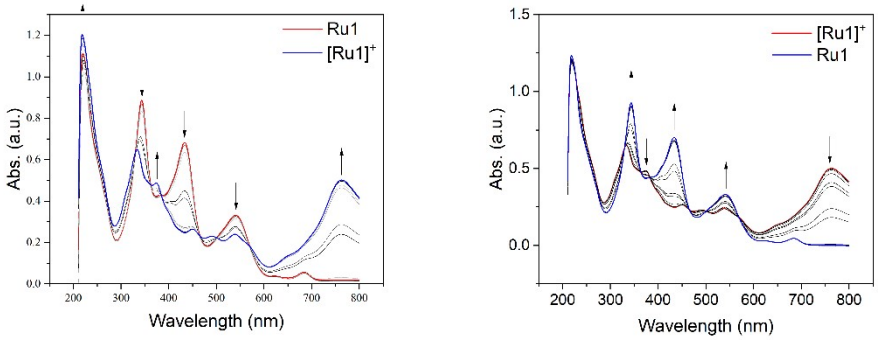

Figure S53: Spectroelectrochemically generated UV-Vis-NIR spectra of **Ru1**. First reversible oxidation (left) and reduction (right). Upon sweeping a bias up to 500 mV and returning down to -300 mV where spectra was recorded at every interval.

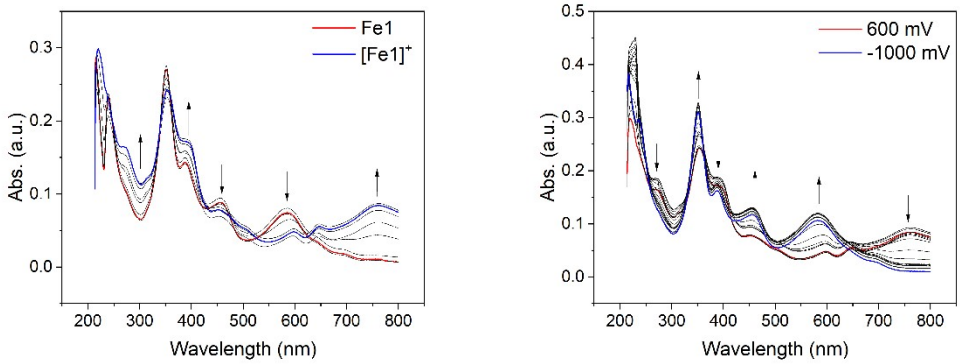

Figure S54: Spectroelectrochemically generated UV-Vis-NIR spectra of **Fe1**. First reversible oxidation (left) and reduction (right) events.

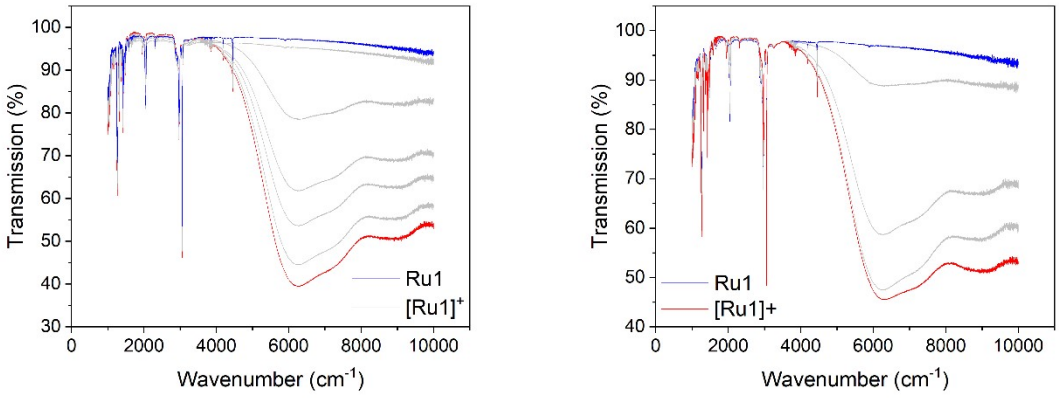

Figure S55: Spectroelectrochemically generated IR spectra of **Ru1**. First reversible oxidation (left) and reduction (right).

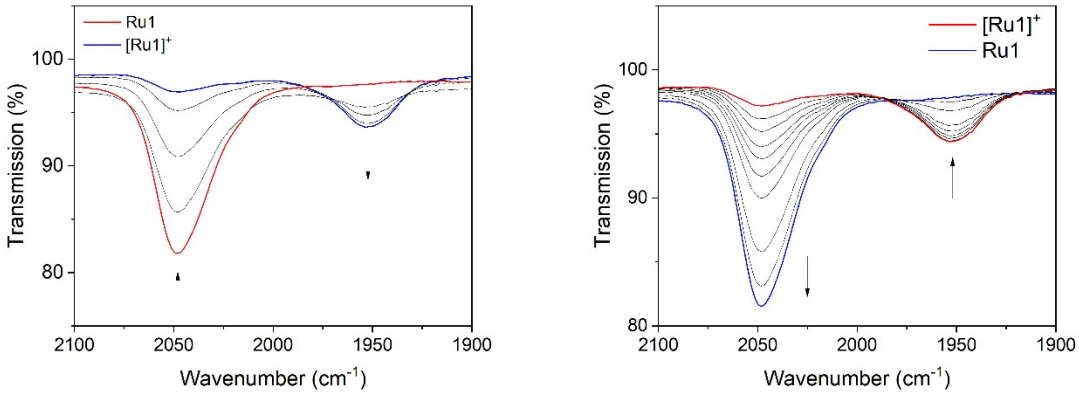

Figure S56: Spectroelectrochemically generated IR spectra of **Ru1** focused on the alkynyl stretches of **Ru1** and **[Ru1]**$^+$. First reversible oxidation (left) and reduction (right).

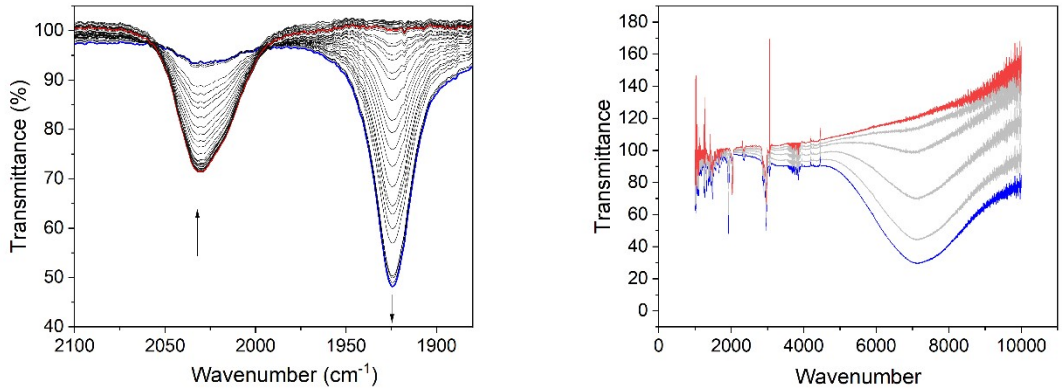

Figure S57: Spectroelectrochemically generated IR spectra of **Fe1** to **[Fe]**$^+$. **Fe1** (red) and **[Fe1]**$^+$ (blue). View of region between 1850 and 2100 cm^{-1} (left) and expanded between 1000 and 10000 cm^{-1} (right).

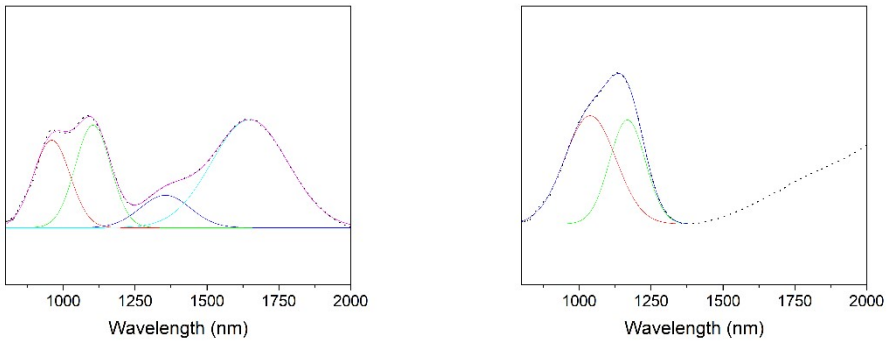

Figure S58: Deconvoluted NIR bands for (a) [**Ru4**]$^+$ and (b) [**Fe3**]$^+$.

Table S4: Deconvoluted Gaussian peaks for **Ru4** and **Fe2**

Compound	Peak	V_{max} / nm (cm^{-1})	Abs	FWHM /cm^{-1}
Ru4	1	960 (10400)	0.211	1628
	2	1103 (9066)	0.243	1188
	3	1355 (7380)	0.092	1117
	4	1648 (6068)	0.256	1159
Fe3	1	1038 (9634)	0.325	1656
	2	1168 (8562)	0.314	912

Acid Switching Studies

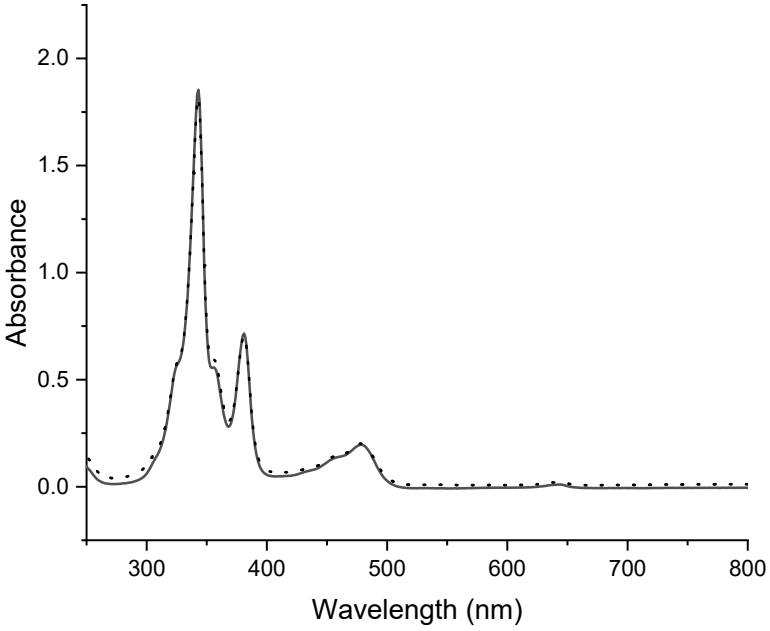

Figure S59 UV-vis spectra of DHP **1** (solid) and after the addition of excess TFA (dotted)

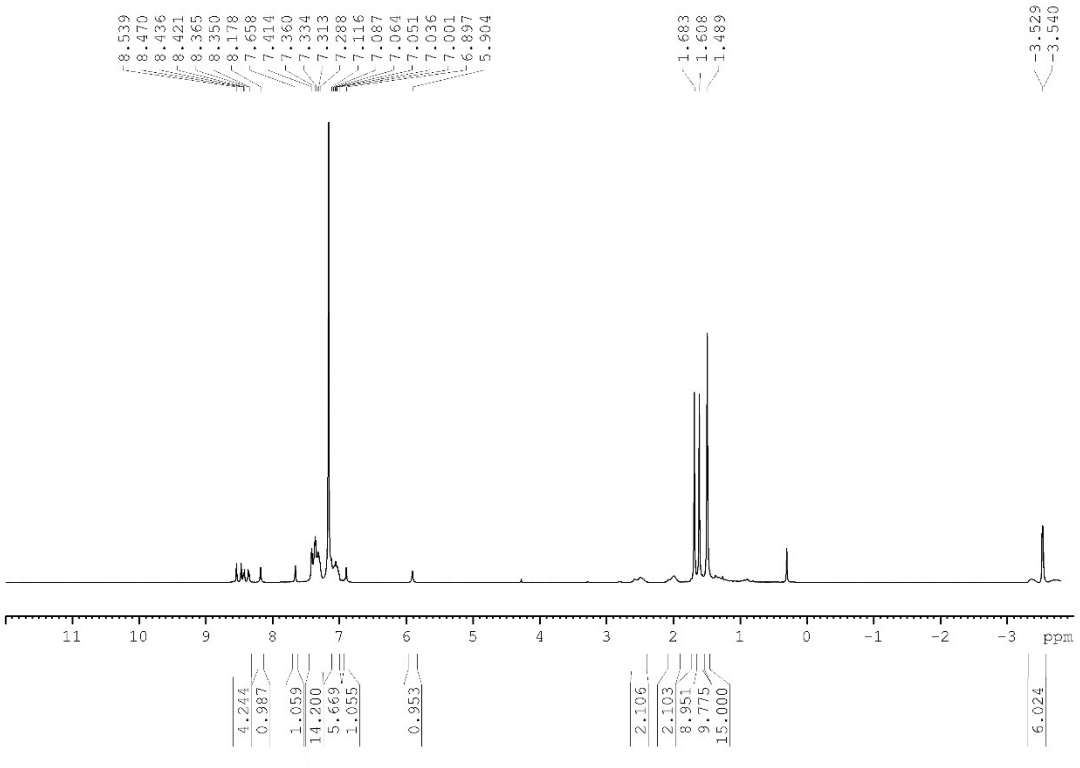

Figure S60 ^{1}H NMR spectrum of **Ru1** and an equivalent of TFA

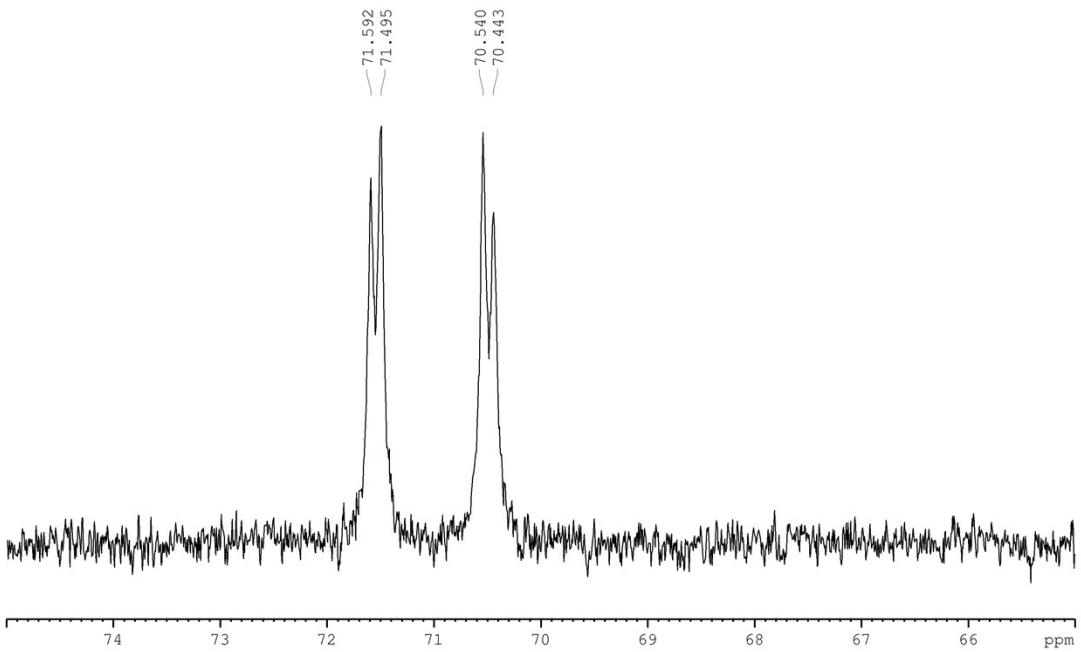

Figure S61 ^{31}P NMR spectrum of **Ru1** and an equivalent of TFA

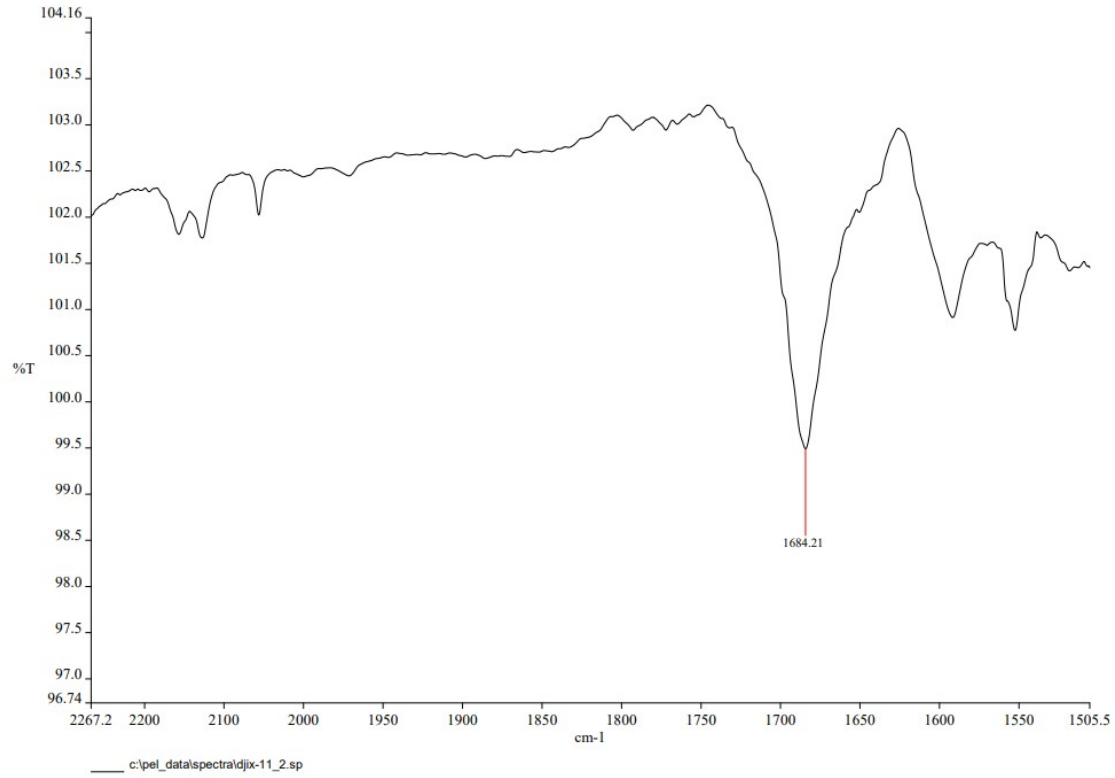

Figure S62 IR spectrum of **Ru1** and an equivalent of TFA

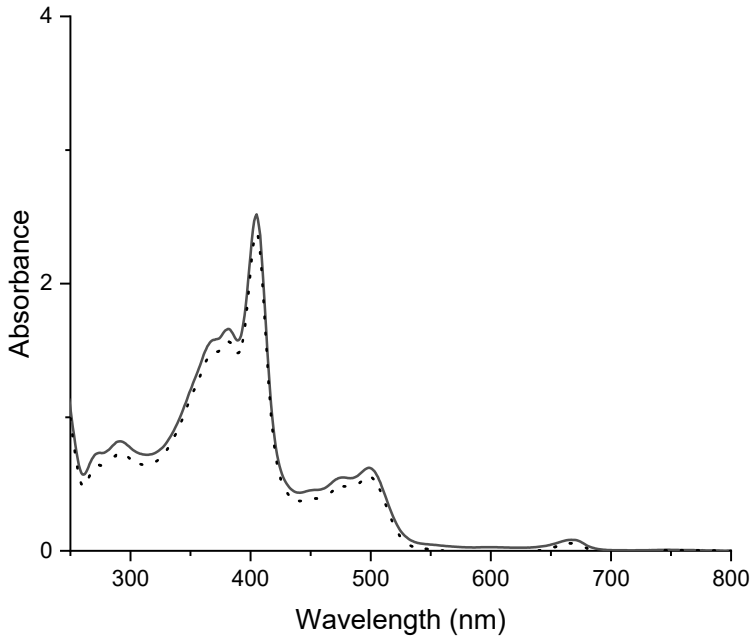

Figure S63 UV-vis spectrum and **Ru1** and an equivalent of TFA before (solid) and after irradiation with visible light for 90 min (dotted)

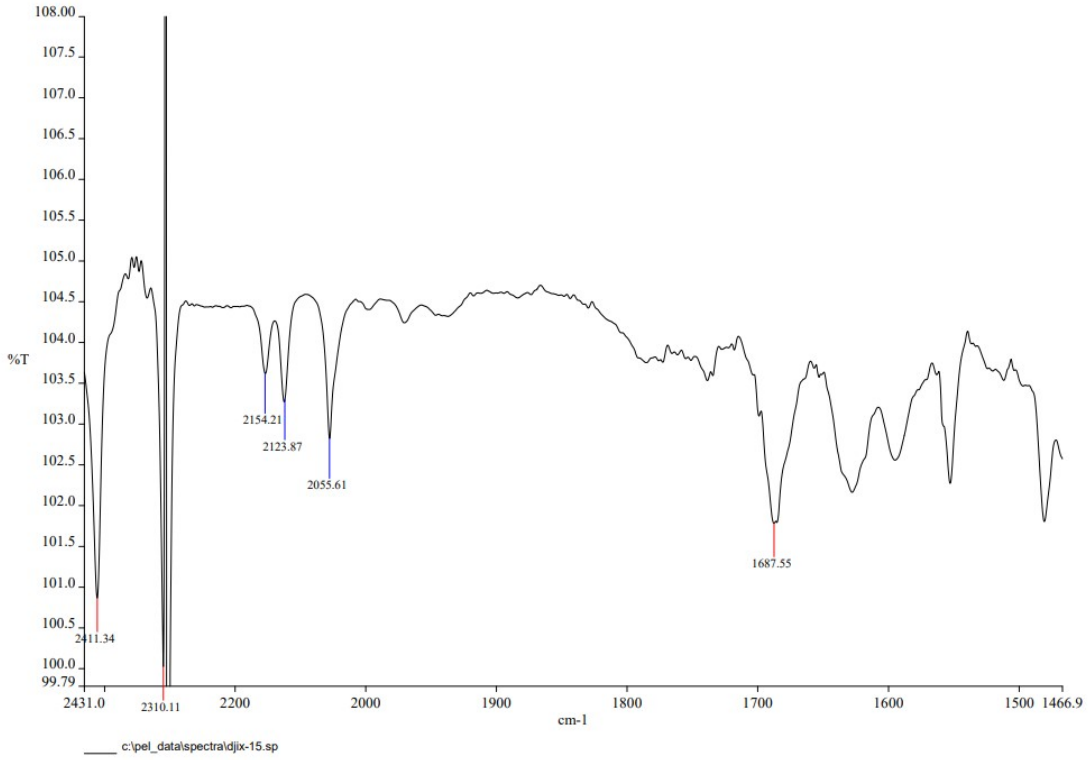

Figure S64 IR spectrum of **Ru2** and an equivalent of TFA

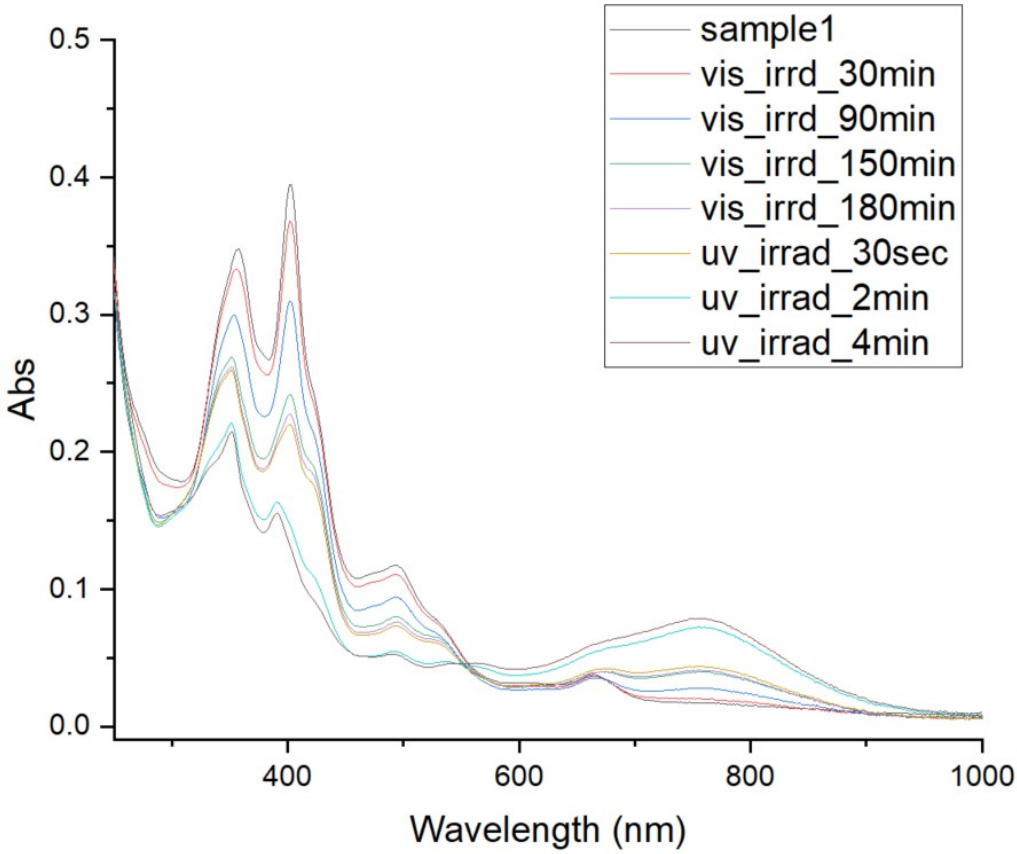

Figure S65 UV-vis spectrum and **Ru2** and an equivalent of TFA before and after irradiation with visible light and UV light

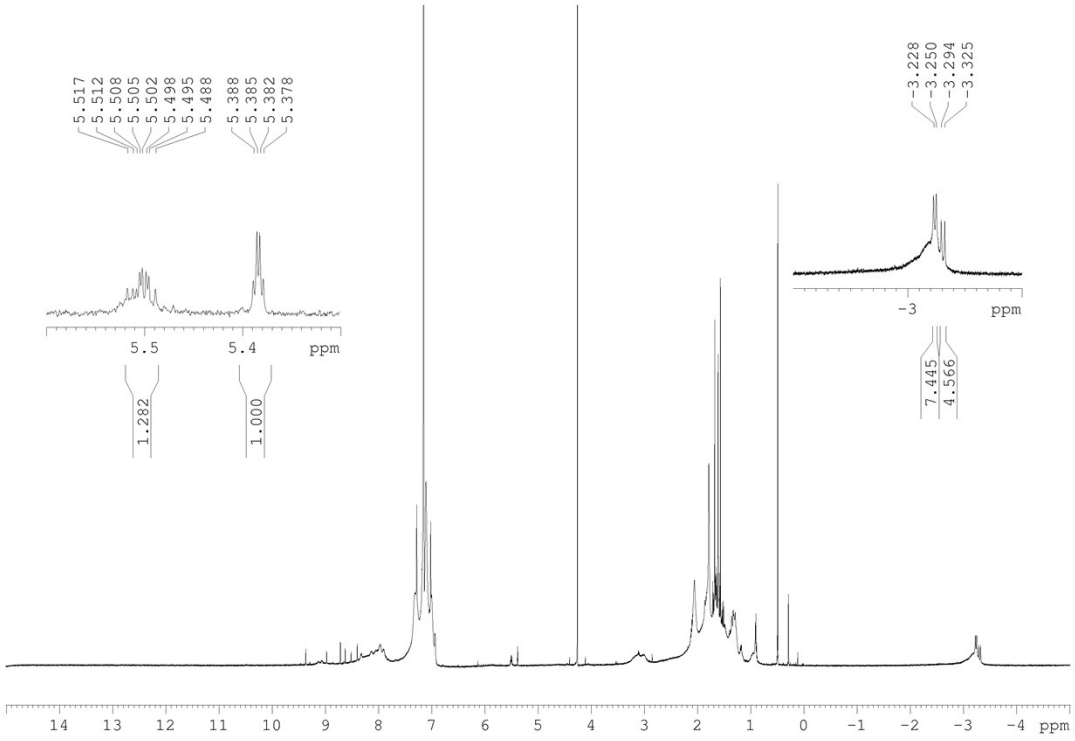

Figure S66 ^{1}H NMR spectrum of **Ru4** and an equivalent of TFA

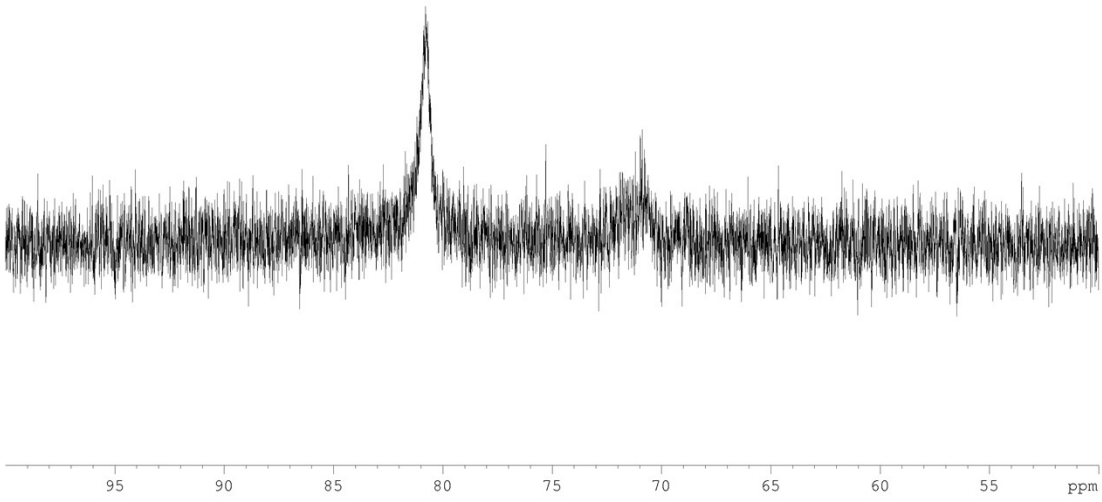

Figure S67 ^{31}P NMR spectrum of **Ru4** and an equivalent of TFA

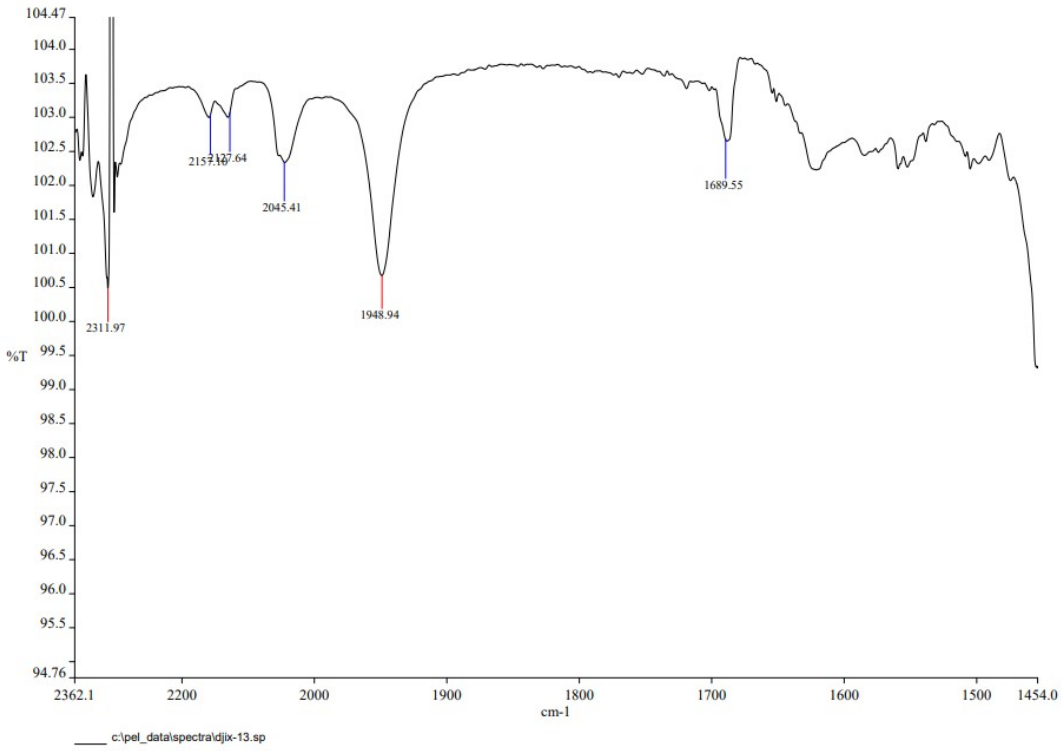

Figure S68 IR spectrum of **Ru4** and an equivalent of TFA

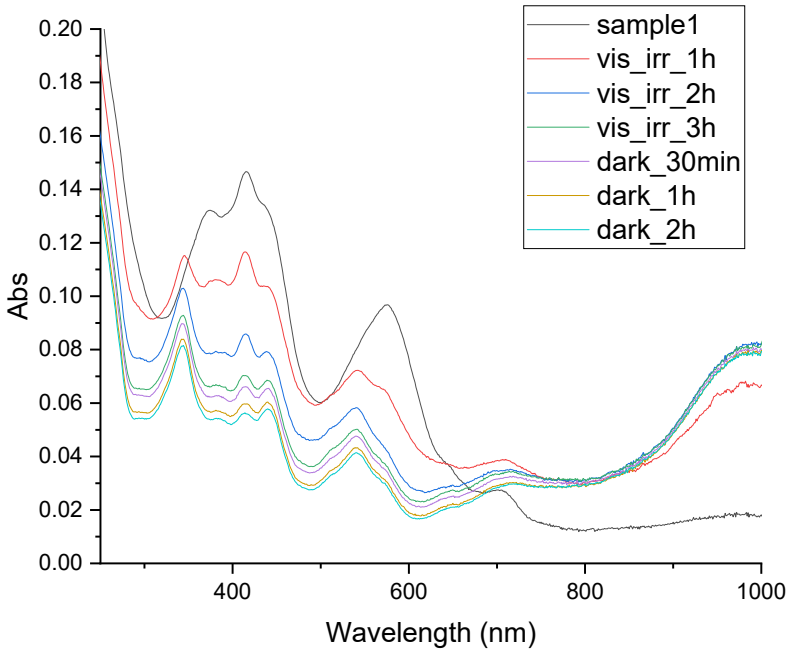

Figure S69 UV-vis spectrum and **Ru4** and an equivalent of TFA before and after irradiation with visible light and UV light

Oxidation Switching Studies

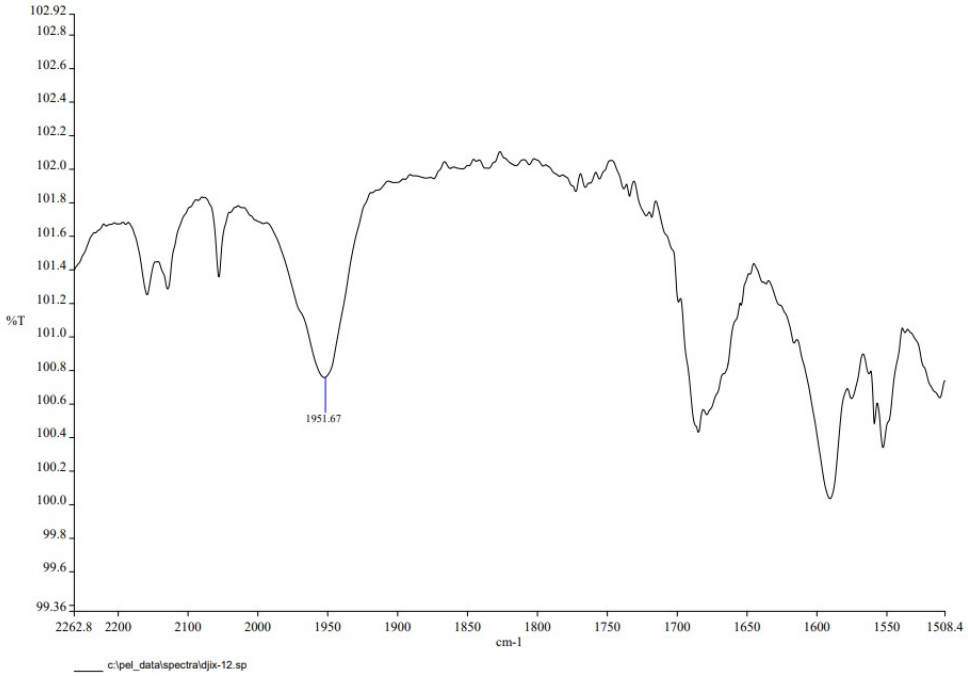

Figure S70 IR spectrum of **Ru1** and an equivalent of $Fc[PF_6]$

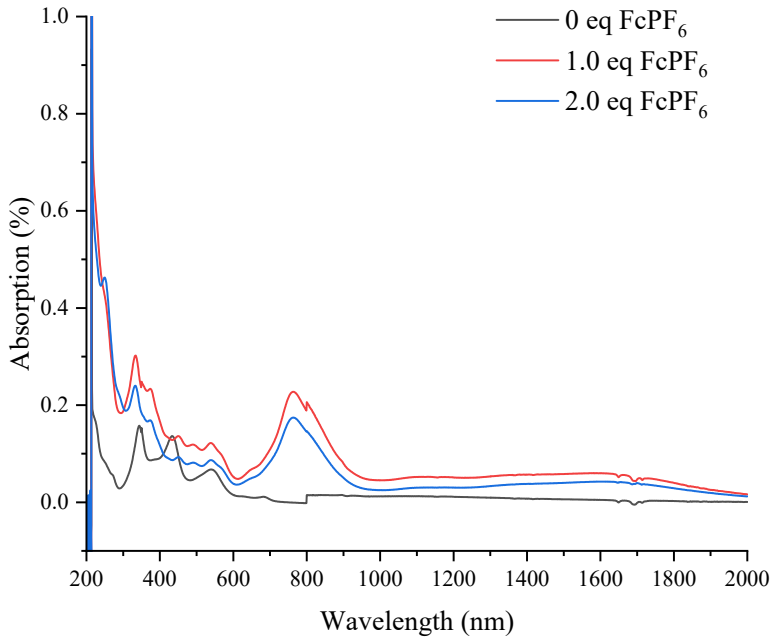

Figure S71 UV-vis spectra of **Ru1** and 1 to 2 equivalents of $Fc[PF_6]$

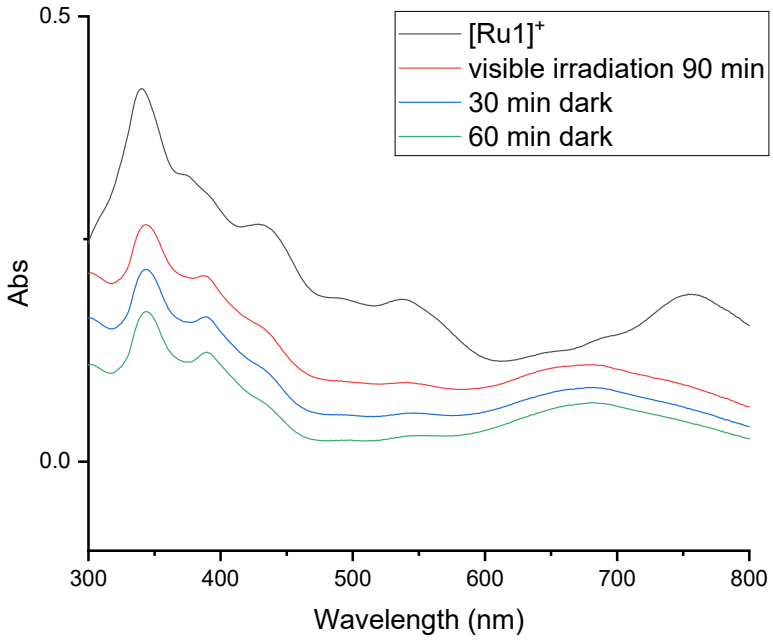

Figure S72 UV-vis spectra of **Ru1** and an equivalent of $Fc[PF_6]$ and irradiation with visible light

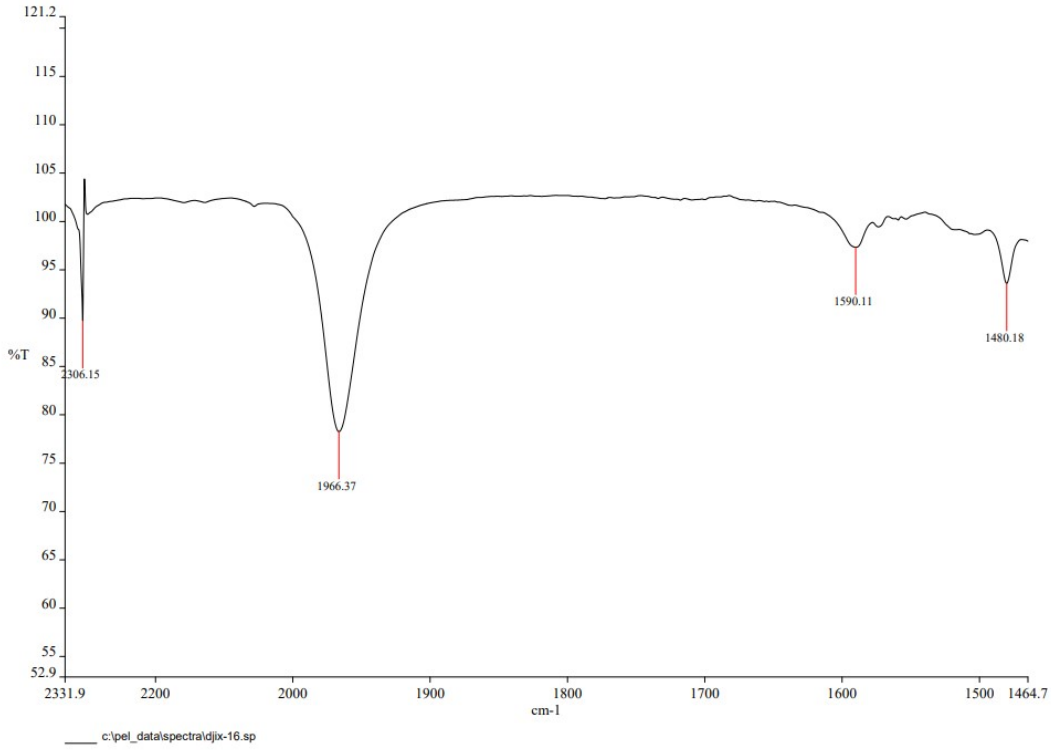

Figure S73 IR spectrum of **Ru2** and an equivalent of $Fc[PF_6]$

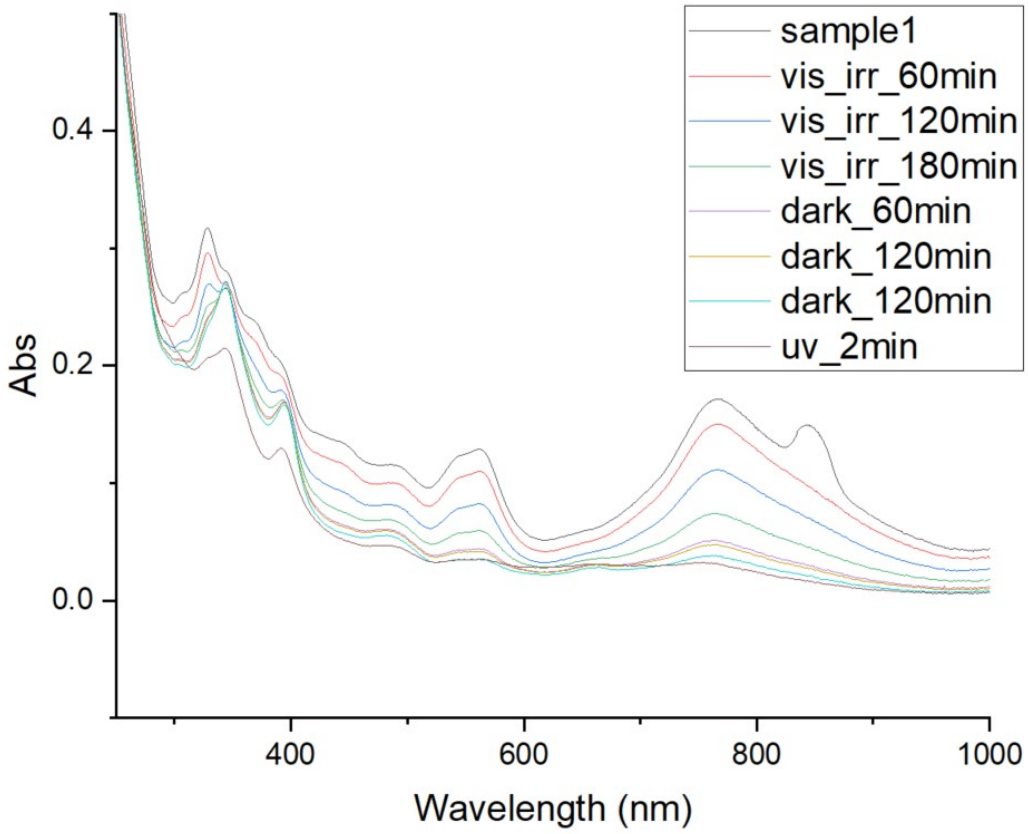

Figure S74 UV-vis spectra of **Ru2** and an equivalent of Fc[PF_6] plus irradiation with visible and UV light

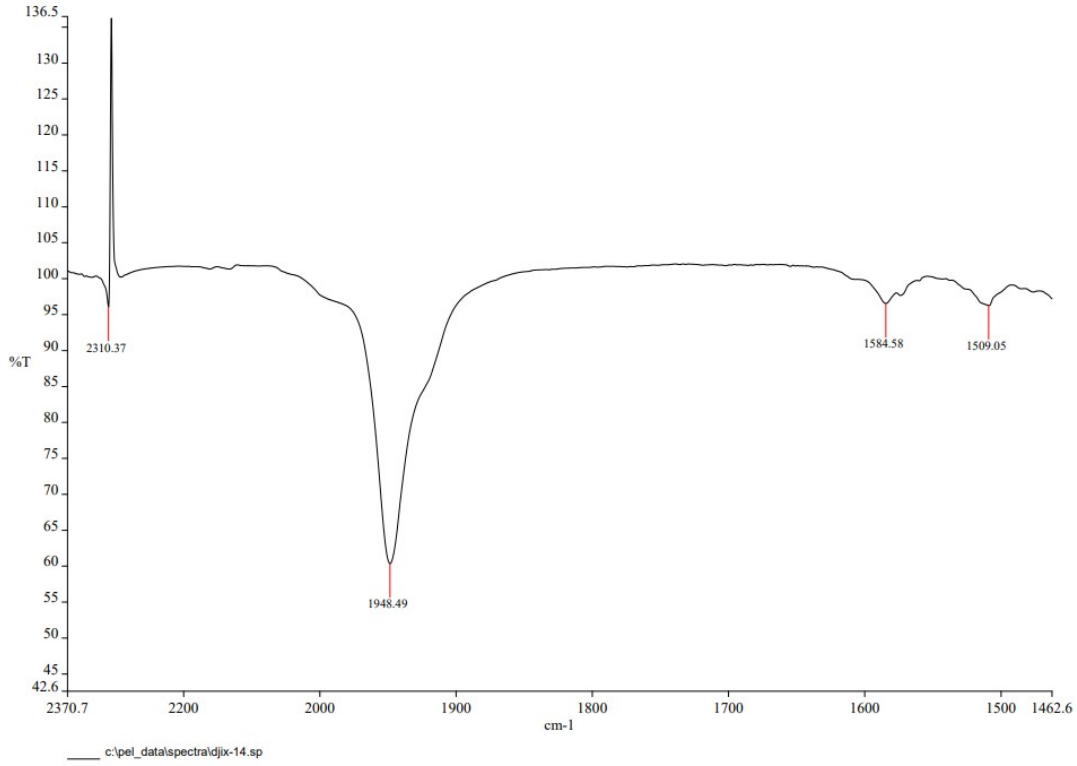

Figure S75 IR spectrum of **Ru4** and an equivalent of $Fc[PF_6]$

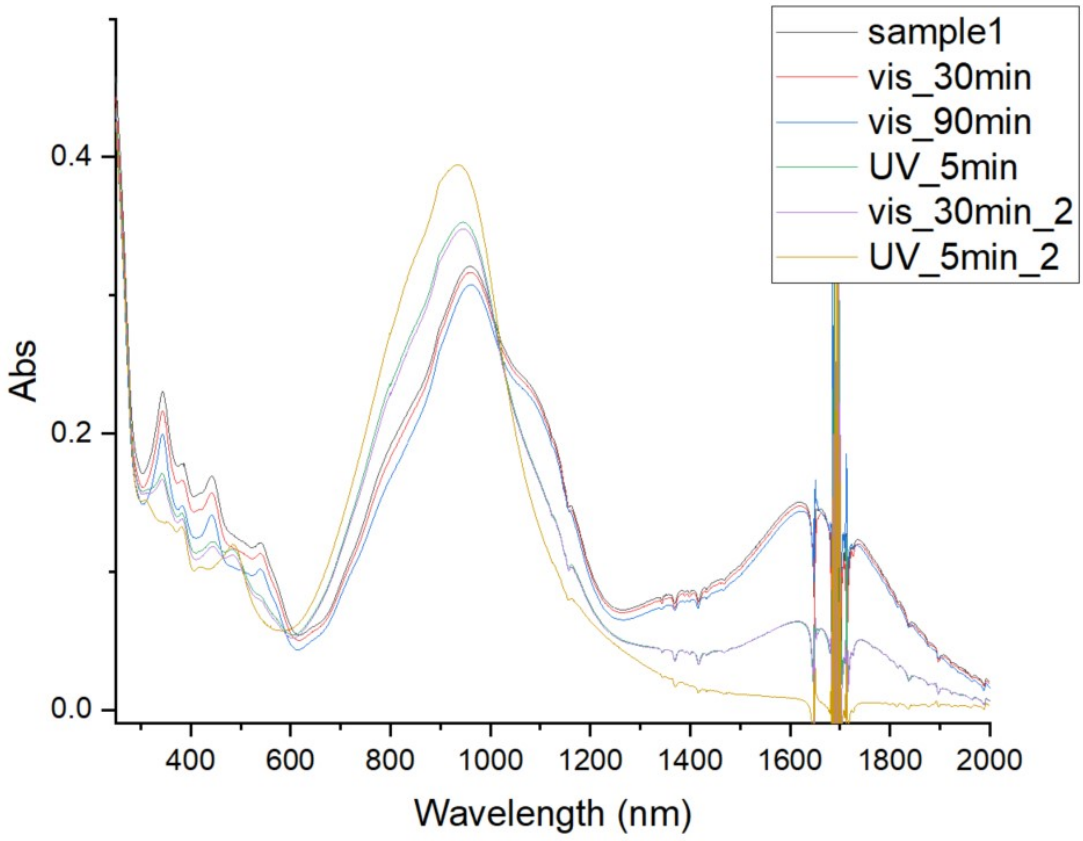

Figure S76 UV-vis spectra of **Ru4** and an equivalent of Fc[PF_6] and exposure to visible and UV irradiation

Theoretical

All calculations were performed with the ORCA[4] computational chemistry package, version 5. Initial geometry optimizations for all systems were conducted using the ωB97M-V[5] density functional approximation using the def2-SVP[6] basis set, followed by subsequent optimizations with the larger def2-TZVP[6] basis set. This approach was employed in order to balance computational cost with accuracy. The starting point for the ring-closed geometries was extracted from the experimental crystal structures for DHP, **4** and **Ru2**.

In order to rationalise the thermodynamics of the ring-opening mechanism, relaxed potential energy surface scans were performed varying the C-C bond length (of the bond which breaks during the ring-opening event) from its length in the ring-closed state (roughly 1.5 Å) to 3.0 Å over 15 steps. For the DHP-monoalkynyl system **4**, the def2-TZVP basis set was used due for consistency with the other geometry optimisations. However, for the organometallic

Ru2 system, the def2-SVP basis set was employed due to computational expense, as these are significantly larger systems. The resulting energy profiles from the relaxed surface scans are provided in Figure S78.

Once these scans were complete, the end point of the scan (where the C-C distance is 3.0 Å) was taken as the starting point for the ring-open geometry optimisations, all of which were performed using the larger def2-TZVP basis set. Molecular orbital isosurfaces for the HOMO and LUMO for DHP, monoalkynyl DHP, Ru1 and Ru2 are provided in Figure S79.

For all four systems in their ring-open and ring-closed conformations, Time-Dependent Density Functional Theory (TDDFT) calculations were performed in order to simulate the UV-visible spectra. Here the ωB97M -V functional was utilized for the organometallic system (**Ru2**), while the SCS-wB88PP86, a double hybrid functional, was used for the DHP-monalkynyl system **4** as it was computationally feasible and has demonstrated excellent results for TDDFT calculations.[7] All TDDFT calculations used the def2-TZVP basis set, with the autoaux setting ‘nroots=15’ (i.e. the number of transitions) and 'maxdim=5' (the Davidson expansion space corresponding to the product of maxdim and numroots). The resulting UV-visible spectra are provided in Figure S80.

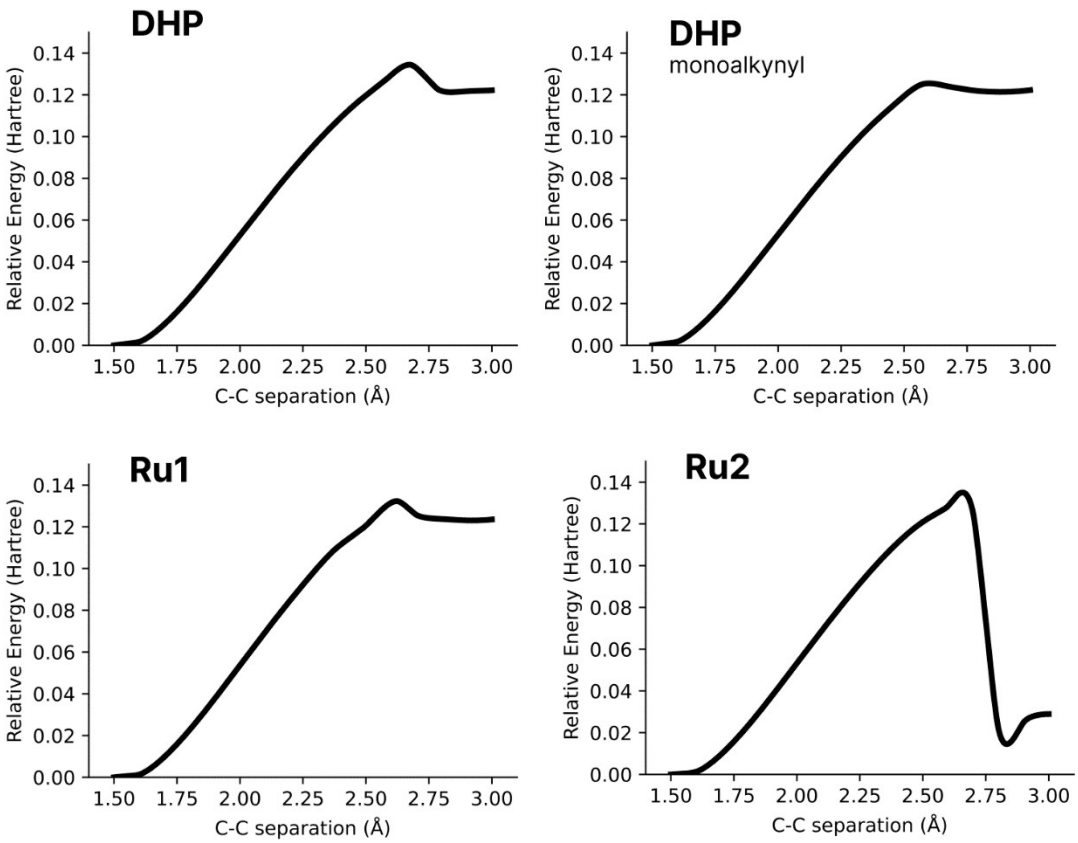

Figure S77 Relaxed surfaces scans of DHP (top left), monoalkynyl DHP (top right), **Ru1** (bottom left) and **Ru2** (bottom right). These plots show the relative energy (y-axis) against the ring-opening C-C distance (x-axis), which has been evaluated by fixing the C-C distance to 15 values over the range of 1.5 - 3.0 angstroms at 15 separate points, then plotted as a continuous line in order to indicate the overall trend/behaviour.

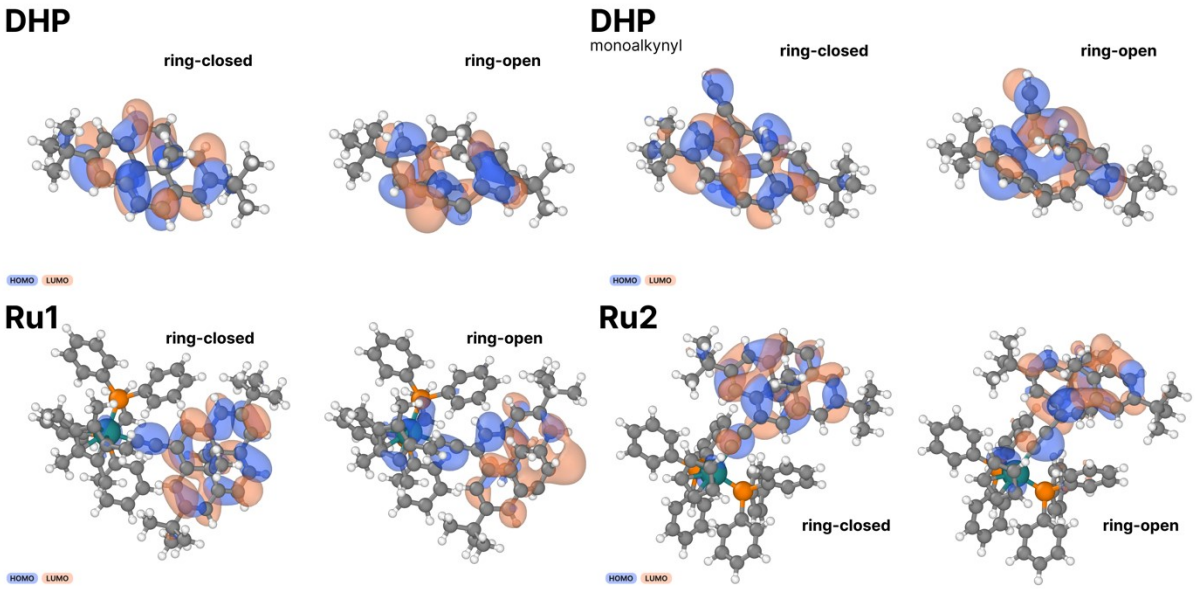

Figure S78 Molecular orbital isosurfaces (0.02au) of the HOMO (blue) and LUMO (orange) for the ring-open and ring-closed forms of DHP (top left), monoalkynyl DHP (top right), Ru1 (bottom left) and Ru2 (bottom right).

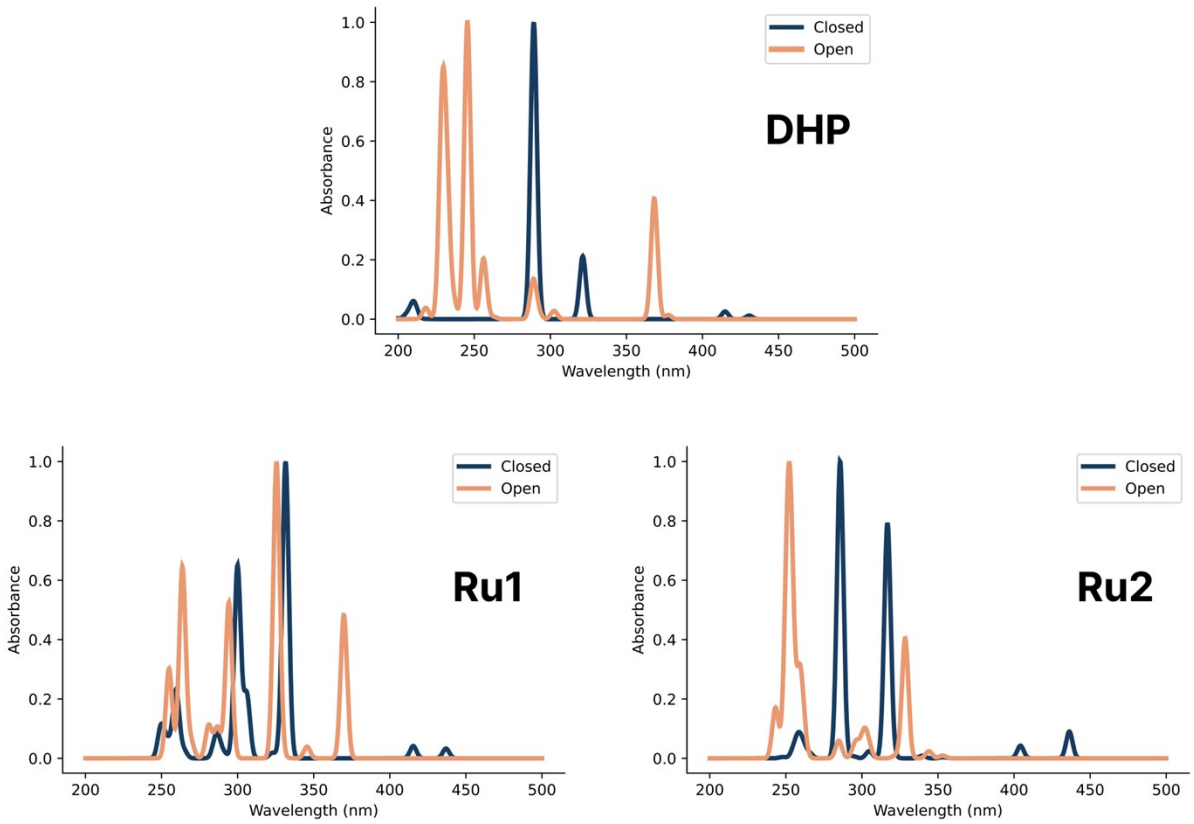

Figure S79 Computed UV-visible spectra for the ring-open and ring-closed forms of DHP (top), Ru1 (bottom left) and Ru2 (bottom right).

References

1. G. Sheldrick, *Acta Crystallogr. A*, 2015, **71**, 3-8.
2. O. V. Dolomanov, L. J. Bourhis, R. J. Gildea, J. A. K. Howard and H. Puschmann, *J. Appl. Crystallogr.*, 2009, **42**, 339-341.
3. G. Sheldrick, *Acta. Crystallogr. C*, 2015, **71**, 3-8.
4. F. Neese, *Wiley Interdiscip. Rev. Comput. Mol. Sci.*, 2022, **12**, e1606.
5. N. Mardirossian and M. Head-Gordon, *J. Chem. Phys.*, 2016, **144**, 214110.
6. F. Weigend and R. Ahlrichs, *Phys. Chem. Chem. Phys.*, 2005, **7**, 3297-3305.
7. M. Casanova-Paez and L. Goerigk, *J Chem Theory Comput*, 2021, **17**, 5165-5186.